Matija Karalic

Characterization of Coupled Microwave Resonator Arrays

Semester Thesis

Quantum Device Lab
Eidgenössische Technische Hochschule (ETH) Zürich

Supervision

Dr. Milan Allan
Prof. Dr. Andreas Wallraff

January 2014

Contents

Abstract

In circuit quantum electrodynamics, superconducting circuits consisting of linear chains of capacitively coupled microwave resonators can be used to realize controlled photon-qubit interactions. For this thesis, I measured and analyzed transmission and reflection in such arrays, focusing on characterizing the coupled resonators. In particular, a system of two coupled resonators without qubits was investigated in detail and the experimental results interpreted based on classical microwave transmission line theory as well as quantum-mechanical input/output theory. I determined characteristic quantities which describe the coupled resonator system, such as resonance frequencies, hopping rates and decay rates, and which form the foundation of understanding more complex phenomena such as the aforementioned photon-qubit interactions that will be implemented in the future. The studied systems are the basis of an ongoing investigation with the goal of detecting Majorana-like modes of light in an optical system.

Chapter 1

Introduction

The coupled resonators studied in this thesis are an experimental realization of circuit quantum electrodynamics (QED). Accordingly, the first section of this chapter briefly introduces the concepts of circuit QED. The section thereafter gives some background information on Majorana fermions and the idea of using circuit QED, or more precisely, linear chains of coupled resonators, to measure Majorana-like modes of light. The final section explains the structure of the investigated samples.

1.1 Circuit QED

Circuit QED is a field of physics which explores the interaction of light and matter in a circuit environment [1]. In the simplest case, a single photon trapped in a superconducting resonator couples to a superconducting quantum two-level system, also referred to as qubit. This situation is depicted in Figure 1.1. The photon-qubit coupling is an electric-dipole interaction. A promising field of application for circuit QED is quantum information processing [2].

Note that in the rest of this report, the terms *resonator* and *cavity* are used interchangeably.

1.1.1 The qubit

The qubit represents an artificial atom-like system with two distinct energy levels. The energy difference between the two levels has a corresponding frequency in the microwave range, typically amounting to several GHz. The qubits used at the Quantum Device Lab are based on superconducting Josephson junctions. Examples include charge, flux and phase qubits. Transmons [3] are a newer type of charge qubits with particularly advantageous properties with respect to sensitivity to noise and scalability.

1.1.2 The resonator

Apart from the qubit, the other crucial part of the system illustrated in Figure 1.1 is the superconducting microwave resonator. It is realized in the form of a several millimeters long coplanar waveguide (CPW) resonator, which is weakly capacitively coupled to external transmission lines, here via gap capacitors. The capacitors play the role of partially transmitting mirrors, in analogy to a Fabry-Pérot interferometer.
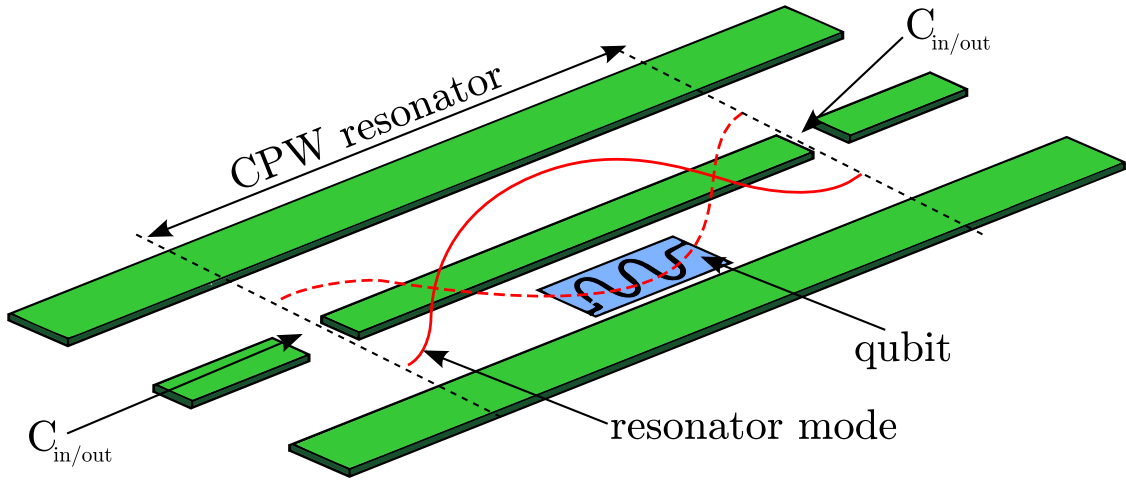
Figure 1.1: Experimental realization of circuit QED. A photon trapped in a capacitively coupled CPW resonator couples to a qubit. $C_{in/out}$ denotes the input/output coupling capacitors, which are assumed to be identical. The resonator mode shown corresponds to the first harmonic: $\lambda = l$, where λ is the photon wavelength and l the resonator length. Not shown are the complete transmission lines leading to respectively away from the resonator. Adapted from Ref. [2].

CPWs have several favorable characteristics with regards to circuit QED such as precisely controllable impedance and large electric fields, meaning stronger photon-qubit coupling [4]. They are fabricated with conventional microfabrication techniques such as photolithography. Because all measurements are taken at low temperatures where the CPW is in a superconducting state, photon losses in the resonator due to absorption are expected to be small.

The coupling to the outside is necessary because the photon-qubit system is studied by measuring the microwave transmission and reflection through the resonator [5]. Even in the absence of a qubit, transmission and reflection measurements can be used to determine important properties of the resonator such as resonance frequencies and photon decay rates due to input/output coupling.

Figure 1.2 shows a simplified equivalent microwave engineering representation of the capacitively coupled CPW resonator without a qubit. The CPW resonator is modeled as a transmission line, which is capacitively coupled to external input/output transmission lines.
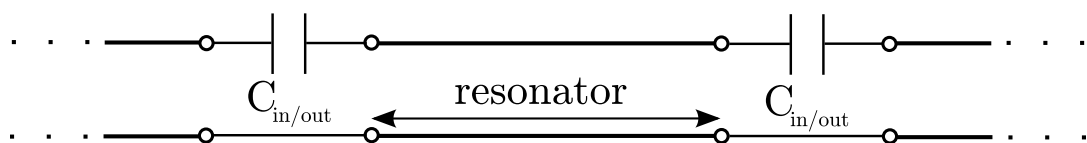

Figure 1.2: Equivalent representation of the system from Figure 1.1, qubit excluded. The lower line may be assumed to be grounded. The dots on either side indicate the external transmission lines.

1.1.3 The photon-qubit system

When the qubit transition frequency is equal to the cavity resonance frequency, the photon and qubit states get mixed together. The result is superposition states that are combinations of photon and qubit states. In the strong coupling regime, the qubit coherently emits and reabsorbs the photon in a phenomenon known as vacuum Rabi oscillation (see, for example, Ref. [6] for more information). The strong coupling regime occurs when the rate of photon emission and reabsorption dominates compared to the photon and qubit loss rates.

1.1.4 Coupled resonator arrays

Coupled resonator arrays are an extension of the system shown in Figure 1.1. Instead of a single resonator with one qubit, they may contain many coupled resonators, each potentially with its own qubit. Like the input/output coupling, the coupling between resonators may also be capacitive. The simplest geometry for realizing an array of coupled resonators is a linear chain, as was the case in my samples. However, researchers have already successfully fabricated two-dimensional honeycomb-like arrays of coupled resonators [7]. Coupled resonator arrays offer the possibility of simulating complex quantum systems in a comparatively accessible fashion [8, 9].

1.2 Majorana fermions

Majorana fermions are fermionic particles which are their own antiparticles. In a recent publication by a group at the Institute for Quantum Electronics at ETH Zurich, the authors suggested a way of experimentally observing Majorana-like modes of light in an optical system [10]. This approach is interesting because, so far, research in Majorana fermions has almost exclusively been conducted in condensed-matter systems such as superfluids and superconductors.

The idea put forward by the authors is based on a one-dimensional chain of coupled cavities, see Figure 1.3. Photons can hop between adjacent cavities. The Majorana-like modes arise due to so-called p-wave photon pairing and can be detected by second order photon cross-correlation measurements at the ends of the chain. Photon bunching is expected to occur as a consequence of the formation of Majorana-like modes.

Additionally, the authors argued that circuit QED is well-suited for implementing their proposal. A linear chain of capacitively coupled microwave resonators with qubits is a favorable realization of the system in Figure 1.3. The number of resonators N should be large.
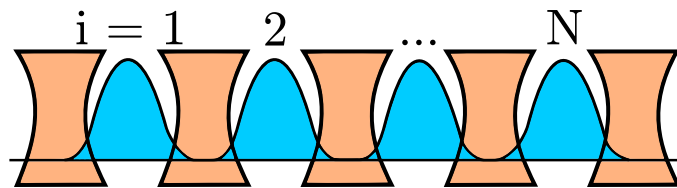

Figure 1.3: Linear chain of N coupled cavities together with a simplified mode. According to Ref. [10].

The Quantum Device Lab at ETH Zurich has decided to pursue the possibility of detecting Majorana-like modes of light using circuit QED. For this purpose, a mask incorporating several coupled CPW resonator systems has been designed [11], and the first wafer fabricated.

1.3 Designed and fabricated samples

The goal of this project was to characterize the coupled resonator systems produced as part of the investigation into Majorana-like modes of light described in the previous section. Let us briefly look at the previously designed and fabricated samples. They ranged from those with $N = 1$ to such with $N = 4$. I concentrated mostly on two samples with $N = 2$, although I also performed measurements on a sample with $N = 4$. Figure 1.4 shows a section of the mask corresponding to a sample consisting of two coupled CPW resonators. Such samples are also known as *dimers*. The symmetric input/output as well as the resonator-resonator coupling are achieved by means of interlocking finger capacitors. The central coupling capacitor enables photons to move from one resonator to the other.

The substrate is a sapphire wafer coated with niobium (white areas in Figure 1.4), which is selectively removed using photolithography (blue areas). The aluminium qubits are written into the designated areas in a separate process using electron beam lithography. Also present are flux lines, charge lines and airbridges. The flux lines are CPWs that can carry a small current which generates magnetic flux in order to tune the qubit transition frequency. The charge lines are CPWs which couple capacitively to the qubit and enable its external excitation using microwave radiation. The airbridges are short, superconducting wires which connect the non-contiguous outside planes of the CPW resonators to each other and so provide a well-defined electrical ground.

Note that resonator chains with $N \leq 4$ do not have a sufficient number of coupled resonators so as to be able to detect Majorana-like modes of light. Chains with $N \approx 10$ are more suited for this purpose. Nevertheless, the shorter chains provide a good starting point for exploring systems of coupled resonators.

The samples studied during this thesis did not contain any qubits. The focus was just on the coupled resonators. Research into transmon qubit integration is ongoing [12].
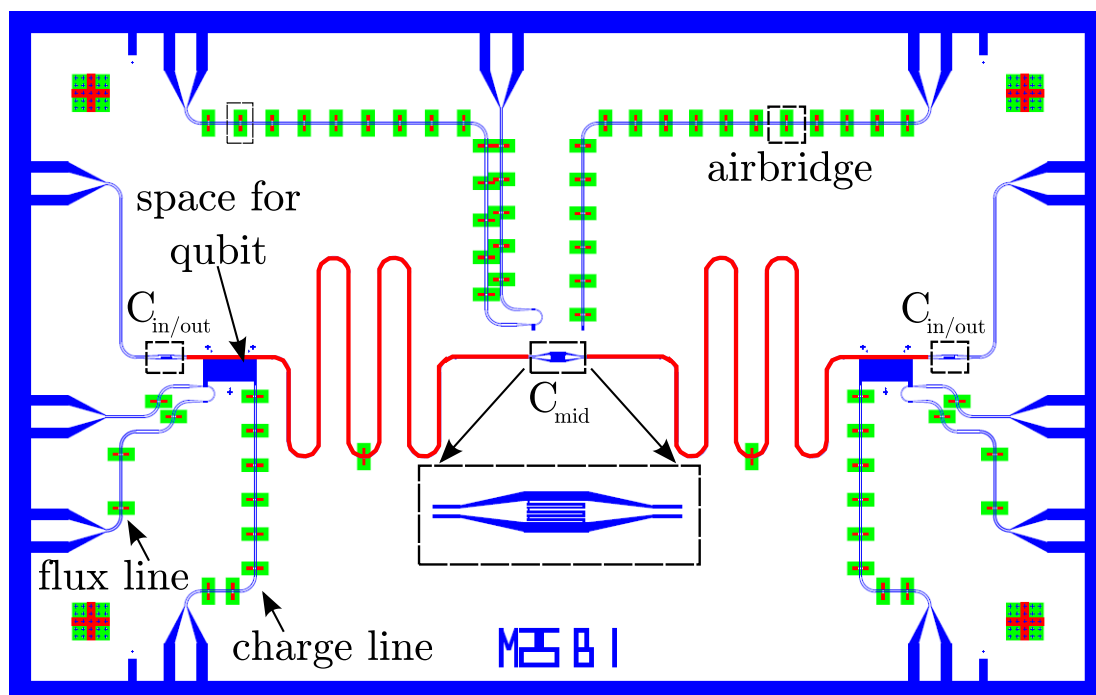
Figure 1.4: Mask cutout of dimer M25 B1. $C_{in/out}$ denotes the identical input/output coupling capacitors and $C_{in/out}$ the middle capacitor. The resonators are highlighted in red. Inset shows a close-up view of the middle capacitor showing the interlocking fingers. Adapted from Ref. [11].

Chapter 2

Theory of transmission and reflection in coupled resonators

This chapter presents a theoretical analysis of transmission and reflection in linear chains of coupled resonators. It begins with a section detailing the way microwave transmission and reflection are measured. Following that, a section is devoted to determining the fundamental resonance frequencies and corresponding modes of a single resonator and of two coupled resonators (dimer). Lastly, two sections explain how to find and interpret complete transmission and reflection spectra from different viewpoints—once using the macroscopic approach of ABCD matrices and once using the microscopic approach of input/output theory.

Most of the terminology and theory in this chapter follow microwave engineering conventions; thus the book *Microwave Engineering* from D. M. Pozar [13] was used as a reference.

2.1 Scattering parameters

A linear chain consisting of any number of coupled microwave resonators can be seen as a two-port network. External input/output transmission lines at the ends of the chain connect the coupled resonator system to the outside and enable its excitation with microwave radiation. Because the single resonator length scales are comparable to the excitation wavelengths (in the millimeter range for microwaves), a description in terms of incident and reflected voltage and current waves is particularly favorable. This description is the basis of transmission line theory. Its justification comes about from solving the *telegrapher's equations*, which are derived from Maxwell's equations.

As mentioned in Section 1.1.2, an individual resonator can be thought of as a piece of transmission line. In this thesis, we are dealing with CPW resonators, but this observation is true for any other kind of microwave resonator such as microstrip.

Figure 2.1 illustrates a linear chain consisting of an arbitrary number of coupled resonators. The two-port network abstraction allows an intuitive way of looking at the transmission and reflection through this system. The two-by-two scattering matrix S relates the voltage waves incident on the ports of the network to those reflected from the ports:

$$\begin{pmatrix} V_1^- \\ V_2^- \end{pmatrix} = \begin{pmatrix} S_{11} & S_{12} \\ S_{21} & S_{22} \end{pmatrix} \begin{pmatrix} V_1^+ \\ V_2^+ \end{pmatrix}, \tag{2.1}$$
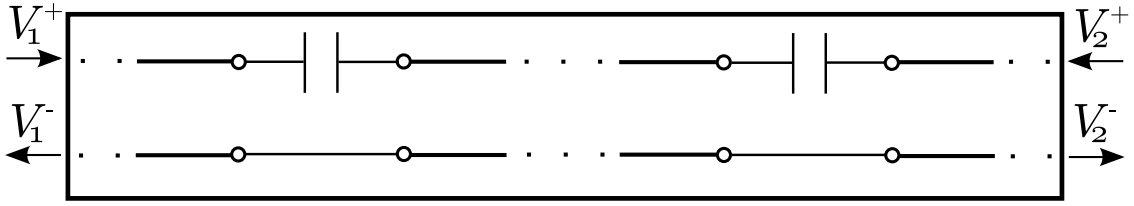
Figure 2.1: A linear chain of coupled resonators viewed as a two-port network.

where V_i^+ is the amplitude of the voltage wave incident on port i and V_i^- is the amplitude of the voltage wave reflected from port i. The elements S_{ij} of S are called scattering parameters and are generally complex numbers. S_{ij} is determined by driving port j with an incident wave of amplitude V_j^+ and measuring the reflected wave amplitude V_i^- coming out of port i. Meanwhile, the port not being driven, in this case necessarily port i, is terminated in a matched load, meaning that there is no incident wave on it. The matrix S completely characterizes the transmission and reflection of the system.

It is possible to prove that, in any reciprocal network, $S_{12} = S_{21}$. A reciprocal network is a network which contains no active devices, ferrites or plasmas. In a symmetric network, $S_{11} = S_{22}$. In a perfectly lossless network, $|S_{11}^2| + |S_{21}^2| = 1$ and $|S_{22}^2| + |S_{12}^2| = 1$, these relations being a consequence of energy conservation.

The coupled resonators that I studied were, by design, both reciprocal and symmetric (see, e.g., Figure 1.4). In reality, the reciprocity condition is indeed fulfilled. However, complete symmetry is impossible because of fabrication tolerances and because the samples are manually glued and wire-bonded to a separate substrate medium and these wires naturally vary in position and length. Similarly, even though all measurements are done at low temperatures where the resonators are superconducting, some losses are still present. Intrinsic resonator losses include resistive, dielectric and radiative losses [14].

In practice, a widespread way of measuring the scattering parameters is by means of a network analyzer.

2.2 Derivation of resonance frequencies

A system of coupled microwave resonators exhibits resonance frequencies, of which there are infinitely many. On resonance, there is maximum transmission and minimum reflection. Off resonance, the transmission vanishes and only reflection occurs. It is possible to derive these frequencies by considering slightly simplified models. This is done below, beginning with the single resonator. Note that we are mainly interested in the fundamental modes and not in the higher harmonics.

2.2.1 Single resonator

The model of the single resonator considered here consists of a lossless, isolated transmission line resonator, see Figure 2.2a. It is also known as an open-circuited $\lambda/2$ line. It is isolated in the sense that there is no input/output coupling. Therefore, the situation is like that depicted in Figure 1.2, where the input/output capacitive coupling has been ignored. This approximation is particularly valid when the capacitance corresponding to the ideally identical input/output capacitors is small (i.e., the coupling is weak). In the investigated samples, this capacitance was on the order of femtofarads. Thus, the picture
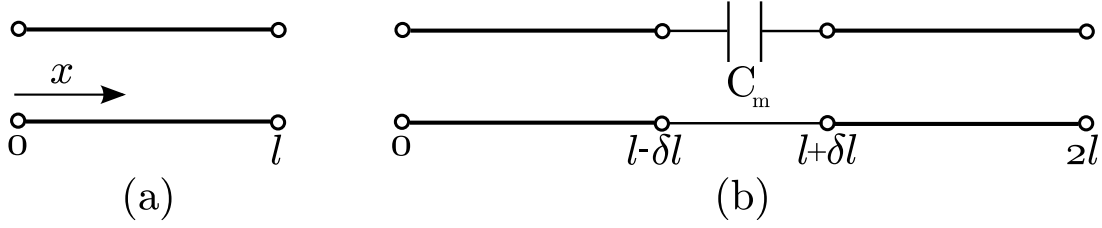
Figure 2.2: Equivalent representation of a single resonator, (a), and of a dimer, (b). δl denotes half of the spatial extent of the coupling capacitor.

of the isolated resonator is reasonable and the results derived in the following are expected to be relevant for the experimental findings. The assumption regarding no losses is just for convenience when looking at the mode waveforms; the resonance frequencies remain the same if losses are considered.

In reality, truly isolated resonators are impractical. In principle however, they could be excited by illuminating them with microwave radiation of a frequency corresponding to a resonance frequency.

Derivation in terms of incident and reflected waves

The voltage and current waves on the resonator of length l can be written in terms of incident and reflected components:

$$V = V^+ e^{-i\beta x} + V^- e^{i\beta x} \tag{2.2}$$

$$I = \frac{V^+}{Z_0} e^{-i\beta x} - \frac{V^-}{Z_0} e^{i\beta x}, \tag{2.3}$$

where V^+ is the incident voltage wave amplitude, V^- the reflected voltage wave amplitude, β the phase constant and Z_0 the characteristic impedance. The open boundary conditions dictate that the current be zero at positions $x = 0$ and $x = l$. From this, it follows that $V^+ = V^-$ and $e^{-i\beta l} - e^{i\beta l} = 0$. The last expression is equivalent to

$$\sin \beta l = 0. \tag{2.4}$$

Equation 2.4 is the resonance condition. The solutions are given by $\beta l = n\pi$, where n is an integer. The fundamental mode ($n = 1$) is described by $\beta l = \pi$ or, equivalently, $\lambda = 2l$, as expected. The associated fundamental frequency f_0 is given by $f_0 = \dfrac{c}{2l\sqrt{\epsilon_{eff}}}$, where c is the speed of light in vacuum and ϵ_{eff} the effective electric permittivity. ϵ_{eff} depends on the geometry of the resonator.

Figure 2.3 illustrates the voltage V and current I waveforms of the fundamental mode.

2.2.2   Dimer

All the assumptions discussed for the single resonator also apply to the case of two capacitively coupled resonators. Additionally, the two resonators of length l are assumed to be completely identical. See Figure 2.2b.

We will see that the presence of the central coupling capacitor leads to a splitting of the eigenfrequencies previously found for the single resonator. The capacitance C_m influences the strength of the splitting.
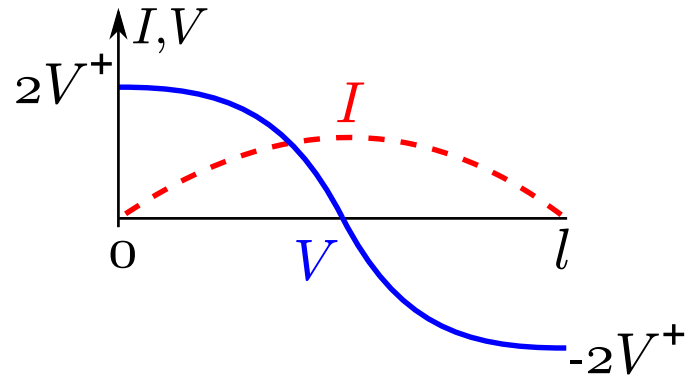
Figure 2.3: Single resonator fundamental mode voltage and current (dashed) waveforms.

Derivation in terms of incident and reflected waves

Now, each resonator has its own voltage and current waves:

$$V_1 = V_1^+ e^{-i\beta x} + V_1^- e^{i\beta x}, \qquad V_2 = V_2^+ e^{-i\beta(x-l)} + V_2^- e^{i\beta(x-l)} \tag{2.5}$$

$$I_1 = \frac{V_1^+}{Z_0} e^{-i\beta x} - \frac{V_1^-}{Z_0} e^{i\beta x}, \qquad I_2 = \frac{V_2^+}{Z_0} e^{-i\beta(x-l)} - \frac{V_2^-}{Z_0} e^{i\beta(x-l)}. \tag{2.6}$$

Note that in this derivation, the transmission lines, i.e., the resonators, are distributed elements, whereas the coupling capacitor is a lumped element. From this viewpoint, the coupling capacitor has no spatial extent. This is hinted at in Figure 2.2b by means of the infinitesimal length segment δl. The left resonator extends from $x = 0$ to $x = l$ and the right from $x = l$ to $x = 2l$ (i.e., $\delta l \to 0$). The voltage and current waves are only strictly defined on the transmission lines. The phase of the waves on the right resonator is arbitrarily chosen such that it is zero at $x = l$.

The open boundary conditions demand that

$$I_1(x = 0) = 0 \tag{2.7}$$

and

$$I_2(x = 2l) = 0. \tag{2.8}$$

The new condition is that the current is continuous at the point $x = l$:

$$I_1(x = l) = I_2(x = l). \tag{2.9}$$

The impedance $Z_m = (i\omega C_m)^{-1}$ of the capacitor connects this current to the voltage difference at the inner ends of the resonators:

$$V_1(x = l) - V_2(x = l) = Z_m I_1(x = l). \tag{2.10}$$

From Equation 2.7, it follows that

$$V_1^+ = V_1^- \tag{2.11}$$

and from Equation 2.8

$$V_2^- = V_2^+ e^{-i2\beta l}. \tag{2.12}$$

It turns out that the single resonator resonance frequencies, given by $\beta l = n\pi$, are also resonance frequencies of this coupled resonator system, independent of the value of C_m.

For $n = 1$, meaning $\beta l = \pi$, it follows from Equation 2.12 that $V_2^+ = V_2^-$. The current at position $x = l$ is equal to zero and therefore $V_1(x = l) = V_2(x = l)$. From this, it follows that $V_2^+ = -V_1^+$. With a given incident amplitude V_1^+, all the other amplitudes are known and the voltage and current waveforms can be visualized, see upper part of Figure 2.4. This $n = 1$ mode of frequency f_0 looks like the first harmonic mode of a resonator of length $2l$. It has a current node at position $x = l$ and thus does not *feel* the coupling capacitor. In this context, it is plausible that the corresponding resonance frequency be independent of C_m.

The derivation of the other resonance frequencies $(\beta l \neq n\pi)$ is a bit more involved. Inserting Equation 2.12 into Equation 2.9 leads to

$$V_2^+ = -V_1^+ e^{i\beta l}. \tag{2.13}$$

Using 2.11, Equation 2.10 takes the form

$$2V_1^+ \cos \beta l - (V_2^+ + V_2^-) = -Z_m \frac{V_1^+}{Z_0} 2i \sin \beta l. \tag{2.14}$$

The term $V_2^+ + V_2^-$ can be rewritten in terms of V_1^+ using Equations 2.12 and 2.13:

$$V_2^+ + V_2^- = -V_1^+ 2 \cos \beta l. \tag{2.15}$$

Inserting the above into Equation 2.14, dividing both sides by V_1^+ and simplifying gives

$$\frac{\omega}{\tan \beta l} = -\frac{1}{2Z_0 C_m}, \tag{2.16}$$

where $Z_m = (i\omega C_m)^{-1}$ has been used. Equation 2.16 is the resonance condition describing the other set of resonance frequencies. In the perfect coupling limit $C_m \to \infty$, the right hand side is zero and the solutions are given by $\beta l = (2n - 1)/2\pi$, n integer. For $n = 1$, the solution is, in terms of wavelength, $\lambda = 4l = 2(2l)$, therefore corresponding to the fundamental mode of a resonator of length $2l$. This makes sense because the perfect coupling essentially means the two individual resonators of length l can be thought of as being one large resonator of length $2l$.

The more relevant case is when the coupling is weak. The solutions to Equation 2.16 then lie around the resonance frequencies found earlier $(\beta l = n\pi)$. Each single resonator resonance frequency splits into two frequencies. To be more precise, for each resonance frequency $\beta l = n\pi$ with some integer n, there is another resonance frequency located slightly below it. Consider now the splitting of the fundamental resonance frequency $w_0 = 2\pi f_0$, i.e., assume that $\lambda = 2l$ at $\omega = \omega_0$ and set $\omega = \omega_0 + \Delta\omega$, $\Delta\omega \ll \omega_0$. Then,

$$\beta l = \pi + \frac{\pi \Delta\omega}{\omega_0} \tag{2.17}$$

and

$$\tan \beta l = \tan \frac{\pi \Delta\omega}{\omega} \approx \frac{\pi \Delta\omega}{\omega_0}. \tag{2.18}$$

Inserting the above into Equation 2.16, observing that $\omega\omega_0 = (\omega_0 + \Delta\omega)\omega_0 \approx \omega_0^2$ and solving for $\Delta\omega$ gives the final result:

$$\boxed{\Delta\omega \approx -\frac{2Z_0 C_m}{\pi}\omega_0^2} \tag{2.19}$$

To summarize, in the weak coupling limit the single resonator fundamental resonance frequency f_0 splits into two fundamental resonance frequencies in the case of two coupled resonators. One of the two frequencies is pinned to f_0, independent of the value of C_m. The second is located slightly below the first (minus sign in Equation 2.19) and the splitting $\Delta\omega$ is directly proportional to C_m. This result is valid when $C_m \ll (\omega_0 Z_0)^{-1}$ (weak coupling). In the investigated dimers, $(\omega_0 Z_0)^{-1}$ was several hundred femtofarads, much larger than the design values for C_m.

The voltage and current waveforms of the two fundamental dimer modes are sketched out in Figure 2.4.

Derivation in terms of RLC resonance

The previous results can also be derived in an alternative, maybe more straightforward fashion by considering that at resonance, the total input impedance/admittance of the coupled resonator system is purely real. Figure 2.5 shows the equivalent circuit of the dimer from Figure 2.2b. Each resonator is replaced by an effective input impedance. It is given by

$$Z_r = -iZ_0/\tan\beta l. \tag{2.20}$$

Equation 2.20 is the input impedance of an open-circuited (load impedance $Z_l \to \infty$), lossless line of length l. The total admittance Y_{tot} of the circuit is then

$$Y_{tot} = 1/(Z_r) + 1/(Z_r + (i\omega C_m)^{-1}). \tag{2.21}$$

Y_{tot} is strictly imaginary. This is a consequence of the fact that the resonators are assumed to be lossless. Setting $Y_{tot} = 0$ and rearranging gives

$$\frac{\omega}{\tan\beta l} = -\frac{1}{2Z_0 C_m}, \tag{2.22}$$

the same expression from before. To check the validity of the other set of solutions, consider that $Z_r \to \infty$ for $\beta l = n\pi$. Then, Y_{tot} is automatically zero.

If losses are not neglected, then in the above derivation β is replaced by $\gamma = \alpha + i\beta$, where γ and α are the propagation and attenuation constants, respectively.

2.2.3   Extension to higher-order systems

An intuitive explanation of the splitting arises when one thinks of the resonators as one-dimensional harmonic oscillators. In a chain of n spring-coupled masses for example (coupling at ends to stationary walls), there are n resonance frequencies, whereas each individual mass spring-coupled to a wall only had one. Therefore, in a system of n coupled resonators, each single resonator resonance frequency splits into n frequencies. Simulations in Microwave Office under weak input/output and resonator-resonator coupling conditions suggest that of the n fundamental resonance frequencies, the highest is always pinned, i.e., independent of C_m, where all the coupling capacitors are assumed to be identical. Additionally, this frequency is practically identical to f_0, the single resonator fundamental resonance frequency. Indeed, one can convince oneself that the single resonator fundamental mode is also an eigenmode of a system with n resonators, $n \geq 2$, where it effectively assumes the role of the $(n-1)$th harmonic and exhibits current nodes at integer multiples of the length l, thus again motivating the apparent independence of this resonance frequency from C_m.
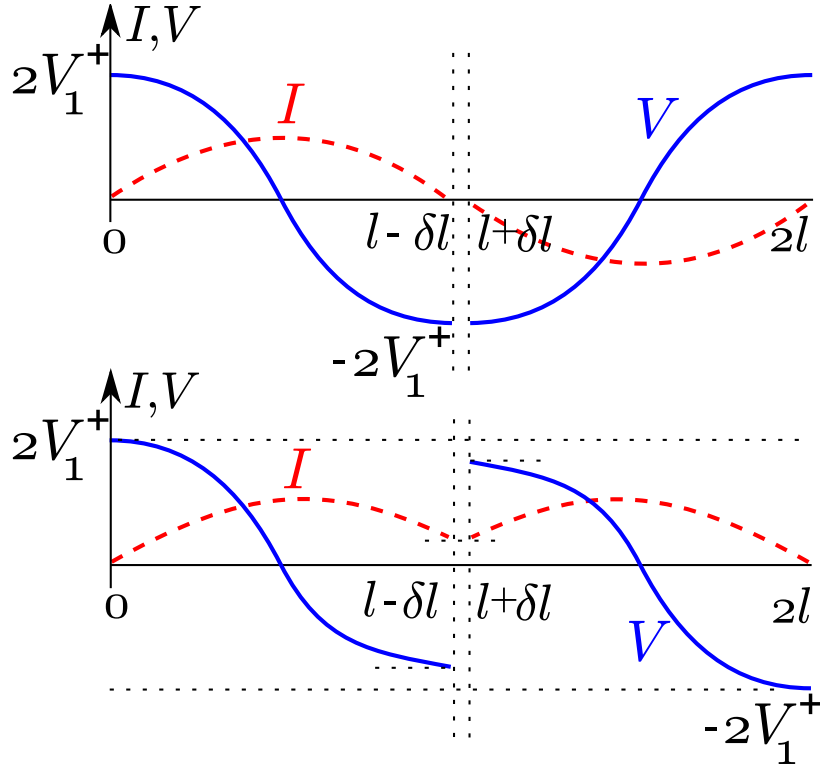
Figure 2.4: Dimer fundamental mode voltage and current (dashed) waveforms. Top mode corresponds to resonance frequency f_0, bottom to resonance frequency $f_0 - \Delta f$.

2.3   ABCD matrices

ABCD matrices, also known as transmission matrices, offer a very convenient way for calculating complete transmission and reflection spectra in two-port networks [13]. This approach originates from microwave engineering and is macroscopic in nature, meaning it describes the coupled resonators in terms of macroscopic quantities like lengths and capacitances.

The ABCD matrix for a two-port network is defined with regards to total voltage and current amplitudes:

$$\begin{pmatrix} V_1 \\ I_1 \end{pmatrix} = \begin{pmatrix} A & B \\ C & D \end{pmatrix} \begin{pmatrix} V_2 \\ I_2 \end{pmatrix}, \tag{2.23}$$

where $V_{1,2} = V_{1,2}^+ + V_{1,2}^-$ and $I_{1,2} = I_{1,2}^+ - I_{1,2}^-$, see Figure 2.1.

The sign conventions for the voltages $V_{1,2}$ and currents $I_{1,2}$ are such that the total ABCD matrix of a cascade connection of two-ports is equal to the product of the ABCD matrices corresponding to the individual two-ports. Concretely, to find the total ABCD matrix of the dimer illustrated in Figure 2.6, it suffices to multiply, from left to right, the matrix $\mathbf{M}_{C_{in/out}}$ associated with the input capacitor with the matrix $\mathbf{M}_r$ associated with the first transmission line and so on:

$$\mathbf{M}_{tot} = \mathbf{M}_{C_{in/out}} \mathbf{M}_r \mathbf{M}_{C_m} \cdots \tag{2.24}$$
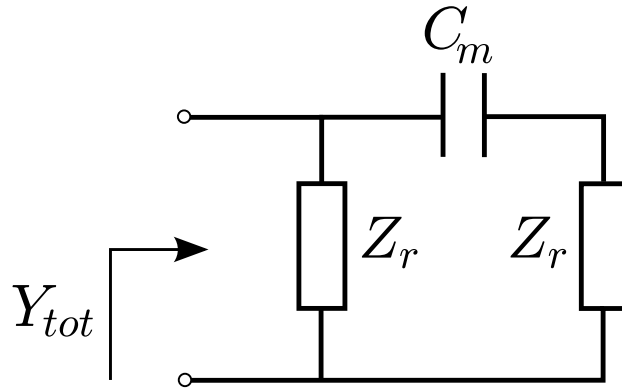
Figure 2.5: Equivalent circuit representation of the dimer.

The extension to longer chains is obvious. $\mathbf{M}_{C_{in/out}}$ is given by

$$\mathbf{M}_{C_{in/out}} = \begin{pmatrix} 1 & Z_{in/out} \\ 0 & 1 \end{pmatrix} = \begin{pmatrix} 1 & (i\omega C_{in/out})^{-1} \\ 0 & 1 \end{pmatrix} \tag{2.25}$$

and $\mathbf{M}_{C_m}$ analogously. $\mathbf{M}_r$ is given by

$$\mathbf{M}_{C_{in/out}} = \begin{pmatrix} \cosh\gamma l & Z_0\sinh\gamma l \\ 1/Z_0\sinh\gamma l & \cosh\gamma l \end{pmatrix} \overset{\alpha\to 0}{=} \begin{pmatrix} \cos\beta l & Z_0 i\sin\beta l \\ 1/Z_0 i\sin\beta l & \cos\beta l \end{pmatrix} \tag{2.26}$$

Once $\mathbf{M}_{tot}$ is known, it can be converted into the equivalent scattering matrix. For example:

$$S_{21} = \frac{2}{A + B/Z_0 + CZ_0 + D}, \tag{2.27}$$

where A, B, C and D are the elements of $\mathbf{M}_{tot}$.

I implemented the ABCD matrix calculation of transmission and reflection spectra of coupled resonators in MATLAB. Reassuringly enough, the results for various resonator configurations were the same as those obtained in Microwave Office. Assuming identical input/output capacitors, coupling capacitors and resonators and that $Z_0 = 50\,\Omega$, as per design of the resonators, the input parameters I used for the model were $C_{in/out}$, C_m, αl and ω_0, where ω_0 is again the single resonator fundamental resonance frequency. By setting these values roughly according to those specified by the design, I could simulate the transmission and reflection in chains of an arbitrary number of coupled resonators. Alternatively, when such spectra are supplied by measurements, one can fit them and extract the abovementioned parameters. It is of course possible to use more parameters
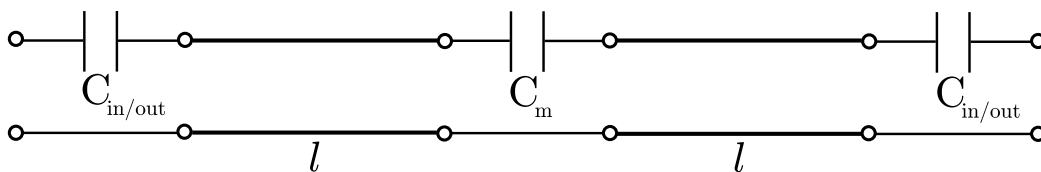

Figure 2.6: Equivalent representation of a dimer, this time incorporating input/output coupling.

and account for asymmetries in the system, parasitic elements etc., but this is only recommended for simulations and not for fitting because increasing the parameter space makes the fitting increasingly difficult.

By varying one input parameter and keeping the rest constant, it is possible to assess its influence on the transmission and reflection. Figure 2.7 depicts the fundamental resonances of $|S_{11}|$ for three different center capacitors. The rightmost dip is actually three curves superimposed on top of each other, demonstrating the pinning phenomenon discussed earlier. Additionally, the splitting Δf is described well by Equation 2.19, see Table 2.1. As expected, the discrepancy between the simulated and calculated values increases for increasing C_m because Equation 2.19 was derived under the assumption of weak coupling.
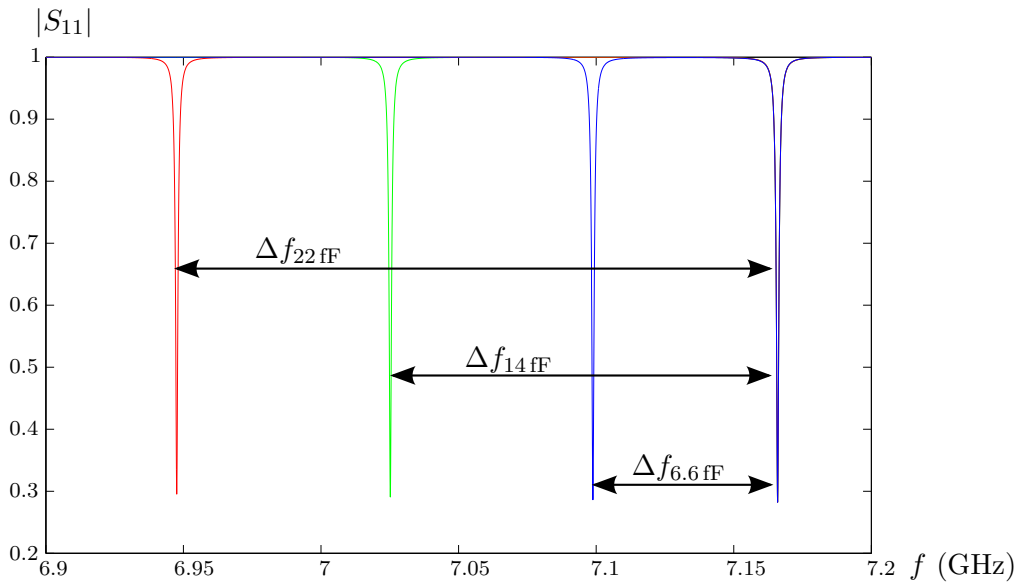

Figure 2.7: Simulated $|S_{11}|$ using ABCD matrices in MATLAB in a dimer for three different values of the capacitance C_m. Other parameters: $C_{in/out} = 6.6\,\mathrm{fF}$, $\alpha l = 8.68 \cdot 10^{-5}$, $f_0 = 7.2\,\mathrm{GHz}$. These parameters roughly correspond to those given by the design. The rightmost dip consists of three curves all lying on top of each other. The fundamental resonances are shown.

Table 2.1: Comparison of simulated (Figure 2.7) and calculated (Equation 2.19) splitting Δf in a dimer for different values of C_m.

C_m	Simulated Δf	Calculated Δf	Relative Error
6.6 fF	67.2 MHz	68.4 MHz	1.8 %
14 fF	140.8 MHz	145.2 MHz	3.1 %
22 fF	218.4 MHz	228.1 MHz	4.4 %

In Figure 2.7, the rightmost resonance frequency is pinned, but not exactly to f_0. The simulation indicates it is pinned slightly below f_0. The reason for this is the input/output coupling. Stronger input/output coupling, i.e, larger values of $C_{in/out}$, lower the upper resonance frequency more with respect to f_0.

If the input/output capacitors are chosen to be asymmetric, then two things happen.

First, the transmission at resonance is not unity, or equivalently the reflection is not zero, even if the resonators are lossless, meaning $\alpha = 0$. An explanation for this phenomenon is given in Ref. [14] for the case of a single resonator: the amount of power flowing out is equal to the amount of power flowing in, in equilibrium. Say the input capacitor is the smaller of the two. If that is the case, the input rate will not be sufficient to sustain the internal voltage, it being drained at a faster rate by the output. To compensate, the input must be driven with a higher amplitude. Because there are no losses, according to energy conservation the rest of the input power is reflected. Second, asymmetry in the input/output coupling results in $S_{11} \neq S_{22}$. Not only that, but the previously symmetric dips of $\Re S_{11}$, $|S_{11}|$ become asymmetric. The same is true for $\Re S_{22}$, $|S_{22}|$. See Figure 2.8.
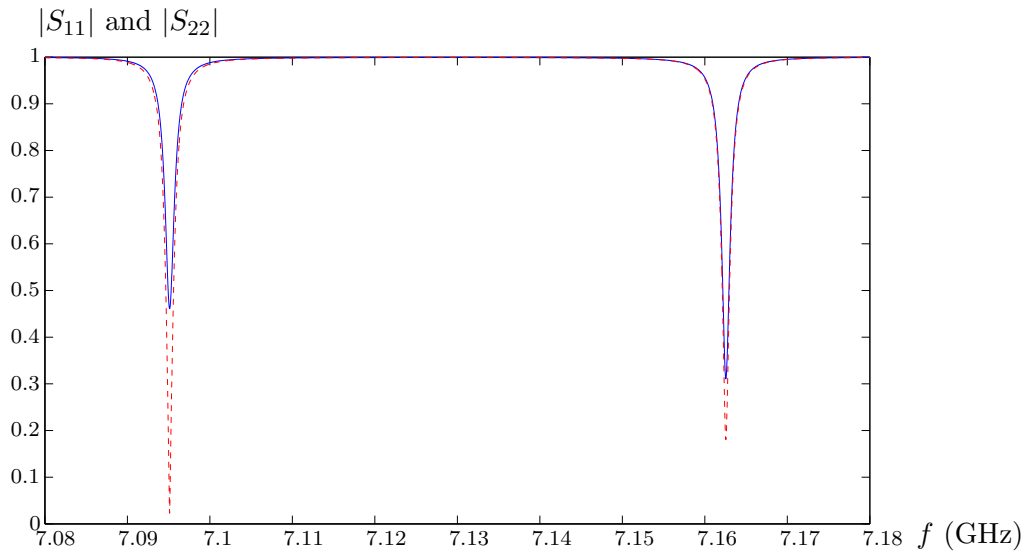

Figure 2.8: Simulated $|S_{11}|$ and $|S_{22}|$ (dashed) in a dimer for the situation of asymmetric input/output coupling. $C_{in} = 6.6\,\text{fF}$, $C_{out} = 8\,\text{fF}$, $C_m = 6.6\,\text{fF}$, $\alpha l = 8.68 \cdot 10^{-5}$, $f_0 = 7.2\,\text{GHz}$.

2.4   Input/output theory

Input/output theory is a quantum mechanical description of coupled optical cavities. It considers coupled cavity dynamics in terms of microscopic decay and hopping rates. For more information on input/output theory, consult Ref. [15].

Figure 2.9 depicts a dimer in the input/output formulation. a, b ($a^\dagger$, $b^\dagger$) are commuting single cavity annihilation (creation) operators. a_{in}, b_{in} (a_{out}, b_{out}) are input (output) field operators. These operators take into account that the resonators are coupled to the outside. J is the photon hopping rate due to the resonator-resonator coupling, mediated in practice by the coupling capacitor.

The Hamiltonian of the system is, considering only fundamental excitations,

$$H = \omega_0 a^\dagger a + \omega_0 b^\dagger b + J a^\dagger b + J b^\dagger a, \tag{2.28}$$

where ω_0 is once again the single resonator fundamental resonance frequency. The resonators are assumed to be identical. The first two terms of H correspond to each resonator individually. The last two terms describe photon hopping from the right resonator to the

left and vice versa. In this case, the cavity dynamics are described by the following differential equations [15]:

$$\dot{a} = -\frac{i}{\hbar}[a, H] - \frac{\kappa}{2}a + \sqrt{\kappa}a_{in} - \frac{\gamma}{2}a \tag{2.29}$$

$$\dot{b} = -\frac{i}{\hbar}[b, H] - \frac{\kappa}{2}b + \sqrt{\kappa}b_{in} - \frac{\gamma}{2}b, \tag{2.30}$$

where κ is the decay rate due to input/output coupling and γ comprises all other decay mechanisms which represent photon losses not due to input/output coupling. The boundary conditions are

$$a_{in} + a_{out} = \sqrt{\kappa}v \tag{2.31}$$

$$b_{in} + b_{out} = \sqrt{\kappa}v. \tag{2.32}$$

The commutators in Equations 2.29 and 2.30 are

$$\frac{1}{\hbar}[a, H] = \omega_0 a + Jb, \qquad \frac{1}{\hbar}[b, H] = \omega_0 b + Ja. \tag{2.33}$$

The strategy now is to write each field operator as a sum of a classical part and a quantum part, see Ref. [16]. Then, the trick is to only consider the classical part, which is just a complex number. Therefore, for the subsequent derivation all operators in the above equations are treated as complex numbers. With this simplification in mind and adopting harmonic time dependence $\partial/\partial t \to -i\omega$, the scattering parameters can be derived. In particular, we have that

$$S_{11} = \left.\frac{a_{out}}{a_{in}}\right|_{b_{in}\approx 0}. \tag{2.34}$$

Skipping all the tedious intermediate steps which contain no additional assumptions, but only consist of manipulating the above equations, the final result is

$$S_{11} = \frac{\gamma^2 - 4i\gamma\Delta\omega - 4\Delta\omega^2 - \kappa^2 + 4J^2}{4J^2 + (\gamma - 2i\Delta\omega + \kappa)^2}, \tag{2.35}$$

with $\Delta\omega = \omega - \omega_0$. In the case of symmetric cavities assumed here, $S_{22} = S_{11}$. Figure 2.10 illustrates $\Re S_{11}$ as well as $\Im S_{11}$ and Figure 2.11 $|S_{11}|$. The two fundamental resonance frequencies are symmetrically split around ω_0. $\Re S_{11}$ and $|S_{11}|$ are symmetric and $\Im(S_{11})$ is antisymmetric around ω_0. The splitting is equal to $2J$. In the lossless case, $\gamma = 0$ and $\Re S_{11}$, $|S_{11}|$ go to zero on resonance.
Equation 2.35 tells us that the two dips in $\Re S_{11}$ are Lorentzians as long as they are distinct and not merged together. This means that, in practice, the decay rates κ and γ can be found by fitting the dips from the experimental measurements with Lorentzians. I took a slightly indirect approach and did not fit the dips, but inverted $\Re S_{11}$ so that
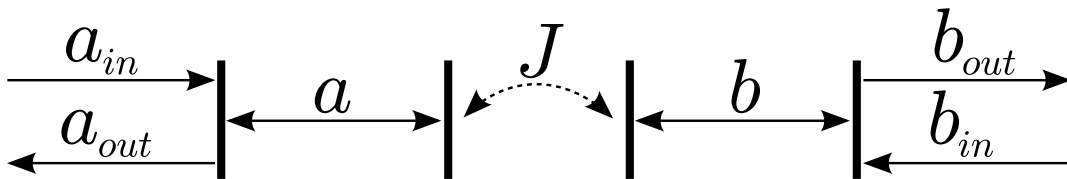

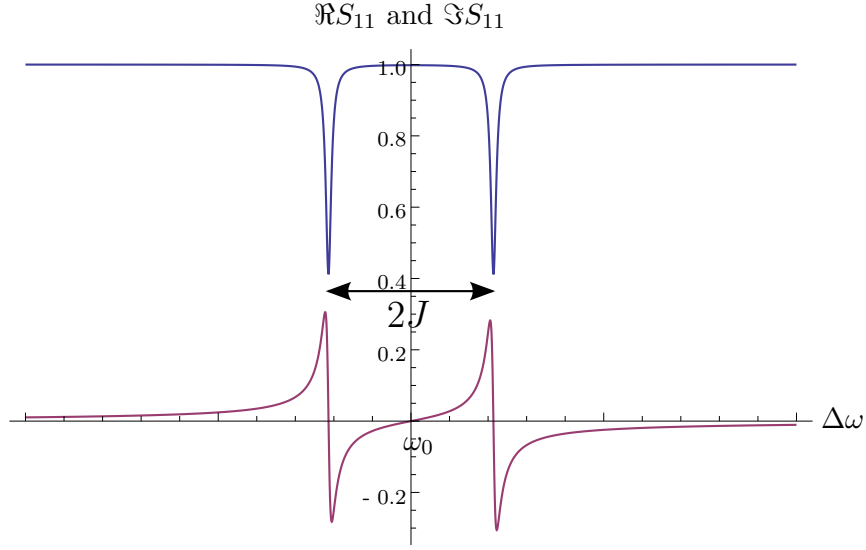Figure 2.9: Dimer model as considered in input/output theory.

Figure 2.10: $\Re S_{11}$ (top) and $\Im S_{11}$ (bottom), from Equation 2.35. Parameters as follows: $J/2\pi = 341\,\text{MHz}$, $\kappa/2\pi = 16\,\text{MHz}$ and $\gamma/2\pi = 11\,\text{MHz}$.

the dips became peaks and the baseline was at zero and not at one (mathematically, I multiplied $\Re S_{11}$ with -1 and added 1). Executing this procedure for the spectrum from Figure 2.10, the result is pictured in Figure 2.12. The peaks are true Lorentzians and no approximations to Equation 2.35 have been made. γ and κ are given by

$$\boxed{\gamma = (1 - max) \cdot FWHM} \tag{2.36}$$

and

$$\boxed{\kappa = max \cdot FWHM} \tag{2.37}$$

max is the maximum and $FWHM$ the full width at half maximum of either of the symmetric Lorentzian peaks in the inverted $\Re S_{11}$. For the quality factor $Q = f/\Delta f$,

$$\boxed{Q \propto \frac{1}{FWHM} = \frac{1}{\kappa + \gamma}} \tag{2.38}$$

Qualitatively speaking, the two resonances are distinct and not merged when their separation is much larger than their widths: $2J \gg FWHM$, i.e., $2J \gg \kappa + \gamma$.

Using Equation 2.19, we arrive to the important result that the microscopic hopping rate J determining the splitting is related to the macroscopic coupling capacitance by

$$\boxed{2J = |\Delta\omega| \approx \frac{2Z_0 C_m}{\pi}\omega_0^2} \tag{2.39}$$

There are two main reasons why it is better to look at reflection instead of transmission. The first is that measured spectra may need to be post-corrected so that the baseline is at the correct position, see Section 4.1.2. The baseline of S_{11}, S_{22} is at one, but that of S_{12}, S_{21} at zero. Therefore, in the case of S_{11}, S_{22} a simple rescaling, i.e., multiplication by a constant factor, is sufficient, whereas as for S_{12}, S_{21} it is not quite clear how to best proceed with the baseline correction. The other reason lies in the fact that reflection measurements give more information about the physical system. Due to the reciprocity
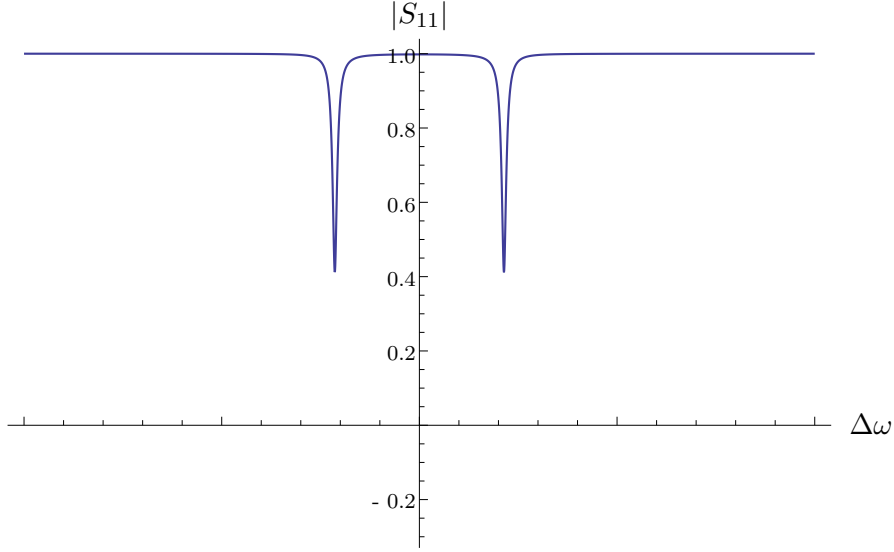
Figure 2.11: $|S_{11}|$, from Equation 2.35. Parameters same as in Figure 2.10.

theorem, see Section 2.1 and Chapter 4 for the experimental confirmation, $S_{12} = S_{21}$ in our samples, independent of any fabrication faults, parasitic elements and so on. However, $S_{11} = S_{22}$ only if the system is symmetric. So by comparing S_{11} and S_{22}, information about the sample (a)symmetry can be extracted.

According to Ref. [14], the quality factor Q is inversely proportional to the mode index. This is one reason why the fundamental modes are more practically relevant than the higher harmonics. In Ref. [14] an expression which connects $C_{in/out}$ and κ is given, similar to Equation 2.39:

$$\omega_0 C_{in/out} Z_0 = \sqrt{\kappa/\omega_0}. \tag{2.40}$$

The model presented above may be expanded. For example, assuming that the input/output coupling is asymmetric, there are then two decay rates κ_a and κ_b. S_{11} becomes

$$S_{11} = \frac{4J^2 + (\gamma - 2i\Delta w - \kappa_a)(\gamma - 2i\Delta w + \kappa_b)}{4J^2 + (\gamma - 2i\Delta w + \kappa_a)(\gamma - 2i\Delta w + \kappa_b)}, \tag{2.41}$$

and S_{22}

$$S_{22} = \frac{4J^2 + (\gamma - 2i\Delta w + \kappa_a)(\gamma - 2i\Delta w - \kappa_b)}{4J^2 + (\gamma - 2i\Delta w + \kappa_a)(\gamma - 2i\Delta w + \kappa_b)}, \tag{2.42}$$

so once again $S_{11} \neq S_{22}$, see Figure 2.13. Note that the splitting in $|S_{11}|$ and $|S_{22}|$ is still symmetric around ω_0.
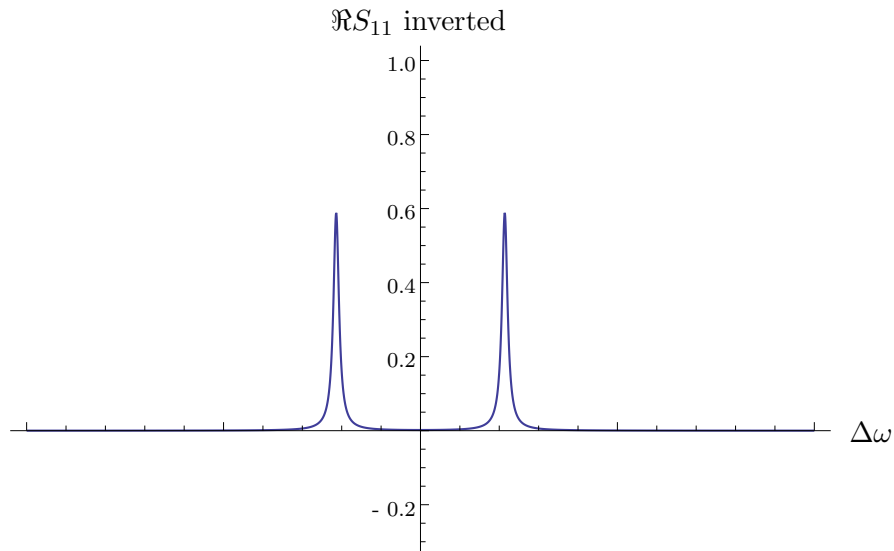
Figure 2.12: Inverted $\Re S_{11}$ from Figure 2.10. By fitting the peaks with Lorentzians, information about the system is obtained.
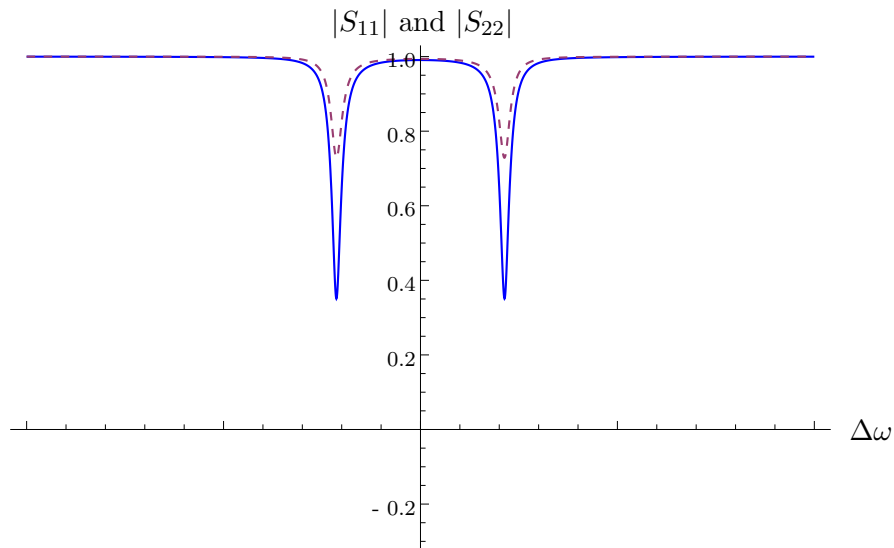

Figure 2.13: $|S_{11}|$ and $|S_{22}|$ (dashed). Parameters as follows: $J/2\pi = 341\,\text{MHz}$, $\kappa_a/2\pi = 80\,\text{MHz}$, $\kappa_b/2\pi = 16\,\text{MHz}$ and $\gamma/2\pi = 11\,\text{MHz}$.

Chapter 3

Experimental setup

The first part of this chapter briefly describes the experimental setup used to perform transmission and reflection measurements on the coupled resonators. The second part explains the calibration procedure. The usefulness of the calibration is discussed in Chapter 4.

3.1 Dipstick setup

The setup which I employed had already been in use at the Quantum Device Lab for a long time and consisted of the well-known dipstick technique. Therefore, this section is purposefully kept concise. For more information, see for example [17].

The samples I measured were provided to me by my supervisor. They stemmed from the first and so far only wafer fabricated according to the design created in a previous thesis [11], see Section 1.3. The investigated samples were M25 A2, M25 B1 and M25 M1, where M25 denotes the mask number, and A2 and B1 were dimers differing solely in the central coupling capacitor. These two samples had 11 ports. M1 was a sample with $N = 4$ and 16 ports, the higher number of ports reflecting the presence of additional flux and charge lines.

For each sample, I soldered two connectors onto a circular $AD1000$ custom printed circuit board. These were the input/output ports. The other ports were left unconnected. Then, my supervisor glued and wire-bonded the sample onto the circuit board. The circuit board was then placed into the protective copper sample holder which was located at the bottom end of the dipstick. The microwave network analyzer $N5230C$ from Agilent Technologies was hooked up to two ports at the top end of the dipstick. Stainless steel coaxial cables running through the hollow dipstick connected these ports to the corresponding sample input/output ports. All these cables were designed to have a characteristic impedance of $50\,\Omega$.

In the case of the samples M25 A2 and M25 B1, the dipstick was lowered directly into a 43 liter wide-neck dewar containing liquid helium at a temperature of roughly $4\,\mathrm{K}$, well below the niobium critical temperature of $9.2\,\mathrm{K}$. It is important to lower the dipstick slowly and step by step so as to allow it to cool gradually, as opposed to lowering it quickly and causing the helium to evaporate in large quantities. An O-ring served to fix the dipstick at a desired depth. The position where the sample became immersed in the liquid helium was clearly observable by looking for a sudden change in the sample transmission and/or reflection, as measured in real-time by the network analyzer. All

measurements were performed with the dipstick inserted as far into the dewar as possible, i.e., with the sample holder at the very bottom of the dewar. Once the measurements were completed, the dipstick was taken out. Again, the dipstick was raised slowly in order to allow it to heat gradually. If it is taken out straight away, a lot of ice forms from the water vapor in the air. This is dangerous because the ice located in small cracks in the solder can lead to the cracks becoming larger, ultimately destroying electrical contacts. Even when the dipstick is slowly taken out of the dewar over a period of 20-30 minutes, some ice is still formed. To melt such ice on the sample holder, a hair-dryer blowing cool air was used.

For the larger sample M25 M1, a different dipstick with larger sample holder was necessary. The dewar employed for measuring the dimers did not have a neck of sufficient diameter to accommodate this sample holder, so a special custom dewar was installed. This dewar, packing a series of thin, circular metal disks serving as heat radiation shielding, needed to be filled with liquid helium from a standard dewar before it could be used. Prior to filling with liquid helium, the custom dewar was first cooled with liquid hydrogen. The actual liquid helium transfer proceeded with more difficulty than expected, failing completely the first time. All the other steps were the same as in the case of the 43 liter wide-neck dewar. Transmission and reflection were measured over frequency in real-time with the network analyzer in the form of two-port scattering parameters. At any desired time, the momentary scattering parameters could be saved for later analysis, either as real and imaginary parts (.csv format) or magnitude, in dB, and phase, in degrees (.s2p format). Measurements with different settings for calibration, input power and time averaging were conducted. Interpolation was set to on, the number of points to 20000 and the IF bandwidth to 200 kHz, unless explicitly stated otherwise. Averaging was useful at low input powers where the signal-to-noise ratio (SNR) was decreased. The averaging process eliminates noise, but is more time consuming.

3.2   Calibration

Calibration was done prior to mounting the sample into the sample holder. The reason for calibration is that the device under test (DUT) is just the sample with the coupled resonators. For instance, the cables connecting the network analyzer to the dipstick and the cables in the dipstick leading to the sample should not be part of the measurement. Calibration ideally enables the network analyzer to remove the influence of the aforementioned cables and any intermediate connectors on the measured transmission and reflection.

The calibration took place at the bottom end of the dipstick with the lower sample holder plate bearing the circuit board removed. Note that because the sample is attached to the printed circuit board, it is impossible to move the reference plane completely to the sample. The connectors and waveguides on the printed circuit board unavoidably influence the measured transmission and reflection.

When no calibration is done, then in the simplest case S_{11} and S_{22} will obtain a frequency-dependent phase factor if one takes into account the cables connecting the DUT to the network analyzer. Therefore, the simplest case refers to a shift in reference plane for each port $n = 1, 2$ by a length l_n of transmission line representing the cables connecting port n to the network analyzer [13]:

$$S'_{nn} = e^{-i2\theta_n} S_{nn}, \tag{3.1}$$

where S_{nn} is the reflection coefficient for port n for the original reference plane, located at $z_n = 0$ (directly at the DUT) and S'_{nn} the new reflection coefficient for the reference plane at $z_n = l_n$ (at the network analyzer). The reference plane for each port n is moved over a length of transmission line l_n from $z_n = 0$ to $z_n = l_n$ due to the cables connecting the DUT to the network analyzer. Because $\theta_n = \beta_n l_n \propto \omega$, the phase offset is directly proportional to frequency. This fact is important for the manual post-correction explained in Chapter 4. S_{12} and S_{21} remain unchanged.

Two different calibration techniques were tried: electronic calibration (ECal) and calibration with a kit. The electronic calibration did not seem to work, seemingly producing even worse measurements. Calibration with a kit consisting of SHORT, OPEN and LOAD (matched impedance, i.e., $50\,\Omega$) devices as well as a THRU connector produced a noticeable improvement in the measurements. Ideally, the calibration should be undertaken at liquid helium temperatures, meaning an individual terminating device or THRU connector is attached, the dipstick lowered, the calibration performed, the dipstick raised, then the next calibration step and so on. Because there are seven steps in total (SHORT, OPEN and LOAD twice for each port, once THRU connecting both ports), this would take the better part of a day. Instead, the calibration was done at room temperature. There exist ways for *in situ* cryogenic calibration which take much less time, see e.g. Ref. [18], but these were not pursued.

When going through the various calibration steps, it is important to know what kind of network analyzer output to expect because it can easily happen that the calibration device is not inserted properly. Refer to Table 3.1 for a summary of the ideal cases for port 1, where port 2 is left as-is (unterminated) except in the case of THRU when both ports are connected. β_1 and l_1 denote phase constant and total cable length for port 1. The situation for port 2 is completely analogous. Figure 3.1 depicts a measurement of the phase of S_{11} during calibration with SHORT (top set of points) and OPEN (bottom set of points) devices. Frequencies below $1\,\text{GHz}$ were not measured; the dotted lines were extrapolated from the available data points above $1\,\text{GHz}$. As the figure indicates, $arg(S_{11})$ decreases linearly with frequency and differs by exactly π for SHORT and OPEN, in agreement with Table 3.1. Additionally, in both cases $|S_{11}| = 1$ (not shown).

Table 3.1: Summary of expected scattering parameters during the calibration procedure. For SHORT, $arg(S_{11}) = \pi - 2\beta_1 l_1$, while for OPEN, $arg(S_{11}) = -2\beta_1 l_1 \propto -f$.

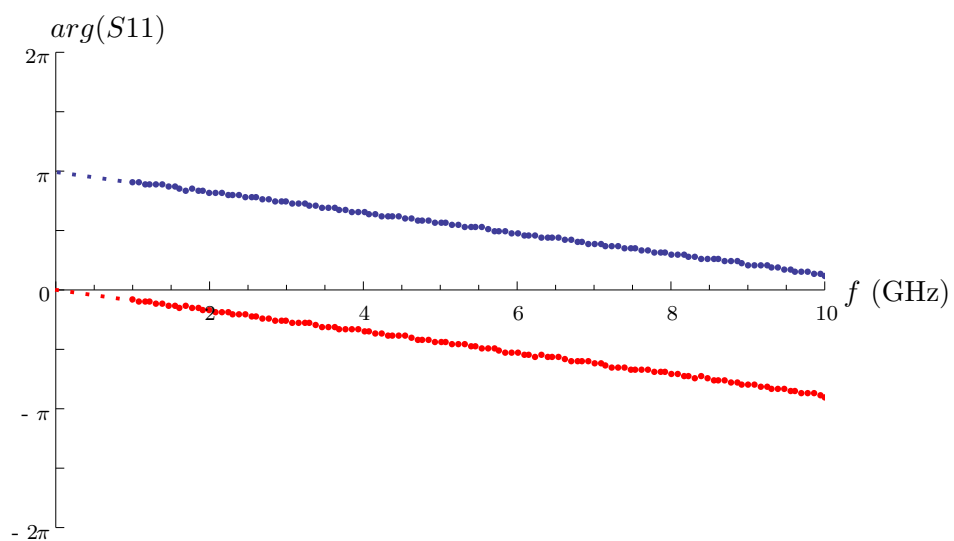| Step	S_{11}	S_{21}
SHORT	$-e^{-i2\beta_1 l_1}$	0
OPEN	$e^{-i2\beta_1 l_1}$	0
LOAD	0	0
THRU	0	1

Figure 3.1: Measurement of phase of S_{11} during calibration with SHORT (top set of points) and OPEN (bottom set of points) devices.

Chapter 4

Results and discussion

In this chapter, the most important experimental results are presented and discussed. The focus is, barring the final section, on the dimers M25 A2 and M25 B1. Only the fundamental resonance frequencies are investigated. The chapter begins with a section explaining the manual post-correction of the raw measurement data and the subsequent fitting. The section thereafter summarizes the information gathered through the fitting. An examination of the observed asymmetry in the scattering parameters follows, including an analysis of potential causes for the asymmetry. Lastly, the final section concerns sample M25 M1 with $N = 4$.

4.1 Measurements and fitting procedure

4.1.1 Uncalibrated and calibrated measurements

Consider first a typical uncalibrated measurement. Figures 4.1 and 4.2 show the real parts, Figures 4.3 and 4.4 the magnitudes of the two-port scattering parameters. $\Re S_{11}$ and $\Re S_{22}$ oscillate strongly, masking the expected resonances. This is consistent with Section 3.2 and Formula 3.1: the oscillations in $\Re S_{11}$ and $\Re S_{22}$ originate in large part from the cables connecting the DUT to the network analyzer. Some oscillations are also present in $\Re S_{12}$ and $\Re S_{21}$, albeit to a much lesser degree. Moving on to the magnitudes, the resonances are clearly visible, although $|S_{11}|$ and $|S_{22}|$ show unexpected oscillatory behavior. These oscillations are most likely standing waves due to reflections created by impedance mismatches at intermediate connections (cables and connectors) between the network analyzer and the DUT. This explanation is in accord with the fact that $|S_{12}|$ and $|S_{21}|$ have no such oscillations when one remembers that S_{ij} is measured with the port not being driven, i.e., port i, terminated in a matched load, meaning there are no standing waves in S_{12}, S_{21}. Lastly, note how the magnitudes of the scattering parameters are often greater than one. This is physically impossible.

Deploying a calibration kit according to Section 3.2 to set up calibrated measurements has profound consequences on the measured transmission and reflection, as Figures 4.5 and 4.6 as well as Figures 4.7 and 4.8 attest. Gone are obvious signs of oscillations. The baselines of $\Re S_{12}$ and $\Re S_{21}$ are at zero, as anticipated. On the other hand, $\Re S_{11}$ and $\Re S_{22}$ are sloped and do not possess well-defined baselines.

The magnitudes of the scattering parameters look as expected, apart from two things. First, despite the calibration, the baselines of $|S_{11}|$ and $|S_{22}|$ are greater than one. This is because the calibration took place at room temperature, the measurements however

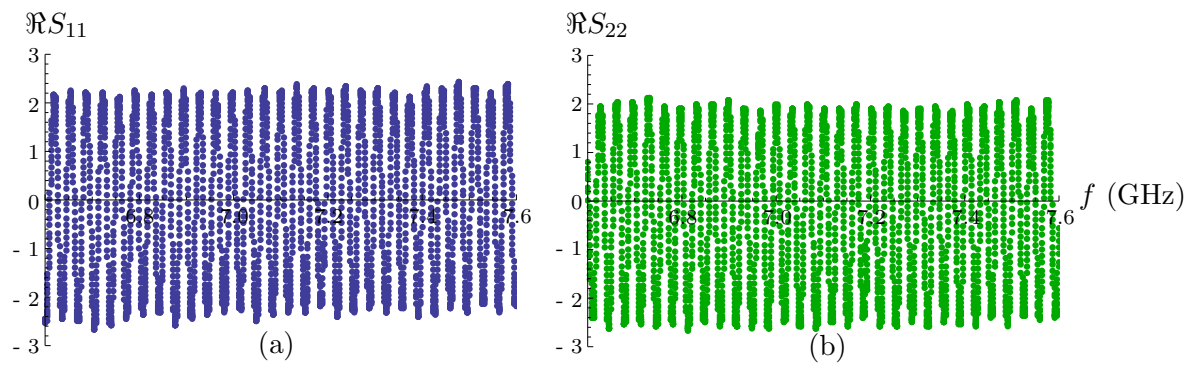Figure 4.1: Measured $\Re S_{11}$ and $\Re S_{22}$ for sample M25 B1. Settings as follows: no calibration, $-2\,\mathrm{dBm}$ input power, averaging off.
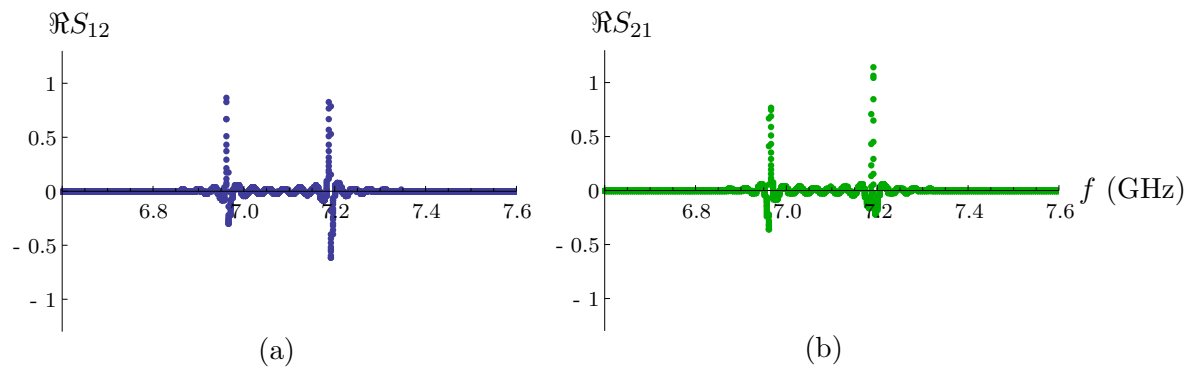

Figure 4.2: Measured $\Re S_{12}$ and $\Re S_{21}$ for sample M25 B1. Settings as in Figure 4.1.
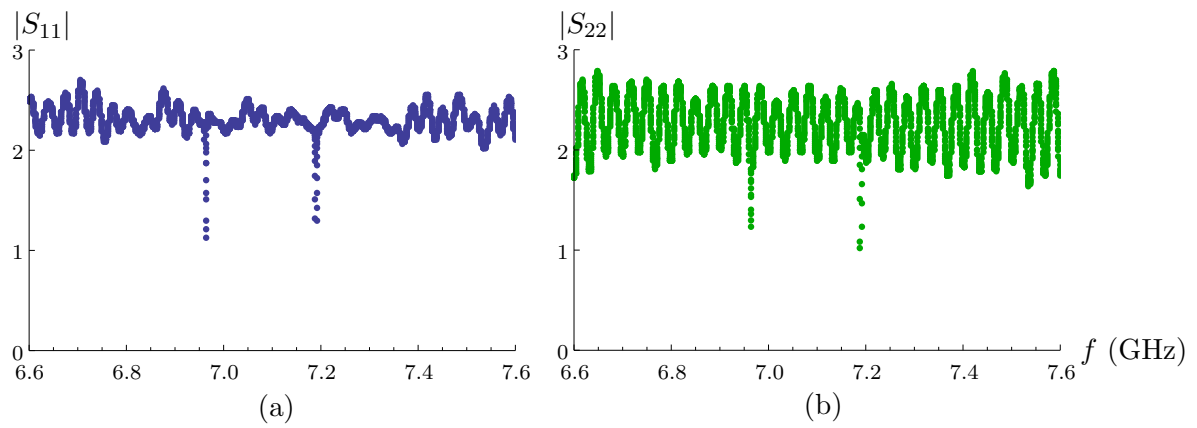
Figure 4.3: Measured $|S_{11}|$ and $|S_{22}|$ for sample M25 B1. Settings as in Figure 4.1.
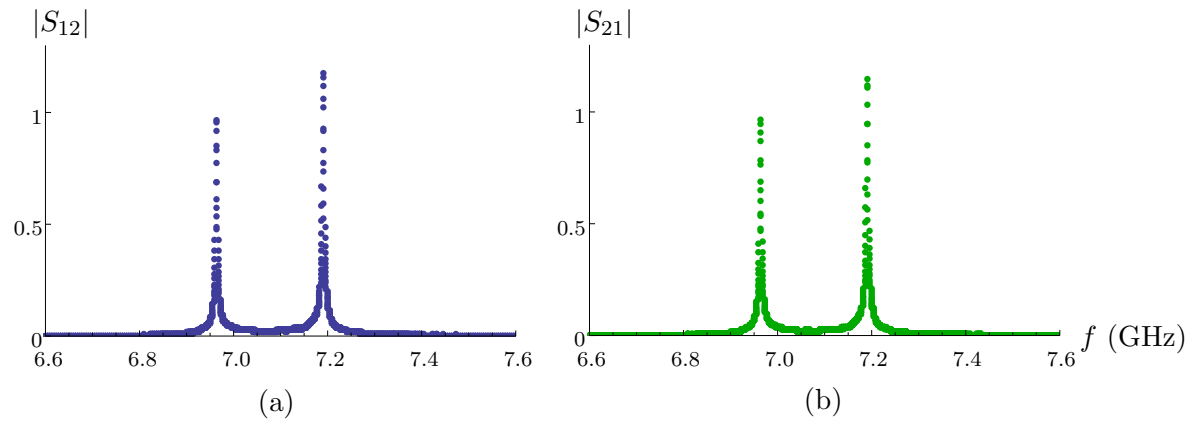

Figure 4.4: Measured $|S_{12}|$ and $|S_{21}|$ for sample M25 B1. Settings as in Figure 4.1.

at liquid helium temperatures where losses are much smaller. For the network analyzer, the smaller losses make it seem like the magnitudes of the scattering parameters can be greater than one. Second, one expects $S_{12} = S_{21}$ due to reciprocity. This is indeed given, since $\Re S_{12} = \Re S_{21}$ and $|S_{12}| = |S_{21}|$. Nevertheless, there is an asymmetry between the two fundamental resonances in S_{12} and S_{21}. One also expects $S_{11} = S_{22}$ due to the sample symmetry, yet the measurements indicate otherwise. There is a marked difference between S_{11} and S_{22}, reminiscent of Figure 2.8. Not only $S_{11} \neq S_{22}$, but again, when considering just S_{11} or S_{22} alone, the two fundamental resonances are asymmetric. All of these asymmetries also occur when no calibration is used, see once more Figures 4.3 and 4.4.

4.1.2 Post-correction and fitting

It turns out that the slopes in $\Re S_{11}$ and $\Re S_{22}$, as evident in Figure 4.5, occur because the calibration is not perfect and fails to completely correct the phases of S_{11} and S_{22}. Therefore, manual post-correction was done on the measurements. The scattering parameters S_{ii}, $i = 1, 2$, were modified according to $S'_{ii} = kS_{11}e^{i(\phi + fp)}$, where k is a real multiplicative constant which shifts the baseline to one, ϕ a constant phase offset, f the frequency and p a real number. Applying the post-correction to the measurements from Figure 4.5 leads to Figure 4.9. Note that it still holds that $S_{11} \neq S_{22}$ and that, in both $\Re S_{11}$ and $\Re S_{22}$, the fundamental resonances are asymmetric. $|S_{11}|$ and $|S_{22}|$ remain unchanged. A negative aspect of the post-calibration is that it was done by hand each time. The phases were corrected until the slopes in $\Re S_{11}$ and $\Re S_{22}$ were judged, by eye, to have disappeared as much as possible. This inherently imprecise procedure degrades the reproducibility of the extracted quantities and contributes to their variance, most notably because the fits can sometimes be quite sensitive to changes in the post-correction.

After the post-correction, $\Re S_{11}$ and $\Re S_{22}$ were ready to be fitted using the model developed within the framework of input-output theory, see Section 2.4 and particularly Equations 2.36, 2.37, 2.38 and 2.39. The reason $\Re S_{11}$ and $\Re S_{22}$ were chosen for fitting is because the analytical fitting function is particularly simple: it is a Lorentzian function as long as the resonances are well-separated, something which was always fulfilled. Both resonances in both $\Re S_{11}$ and $\Re S_{22}$ were inverted and fitted individually with the same function. J is determined by the difference of the two resonance frequencies, $J = \frac{1}{2}(f_{res,2} - f_{res,1})$. The single resonator fundamental resonance frequency, f_0, is, according to Section 2.2, approximately given by the right resonance frequency: $f_0 \approx f_{res,2}$. As an example, Figure 4.10 depicts the final result of fitting the left resonance in $\Re S_{22}$ from Figure 4.9. The extracted quantities from this fit are $f_{res,1} = 6.96\,\text{GHz}$, $\kappa/2\pi = 0.91\,\text{MHz}$ and $\gamma/2\pi = 1.51\,\text{MHz}$.

It is also possible to fit the measured scattering parameters with ABCD matrices. The difference is that, with ABCD matrices, there do not exist simple analytical formulas which can be used for fitting. For a given quantity such as $|S_{11}|$, it is not possible to isolate the resonances, but rather the whole spectrum is fitted at once. Because $S_{11} \neq S_{22}$ and the measured scattering parameters feature asymmetries, fitting with the parameters $C_{in/out}$(assuming $C_{in} = C_{out}$), C_m, αl and ω_0 fails because these parameters only describe the ideal case of symmetric samples. Attempts at trying to introduce additional parameters to better fit the measurements were not particularly successful. Introducing more parameters increases the parameter space and makes the fitting procedure unstable in the sense that it becomes very dependent on the initial guesses. When it does work, some parameters, for example $C_{in/out}$ or C_m, are often completely different than what is
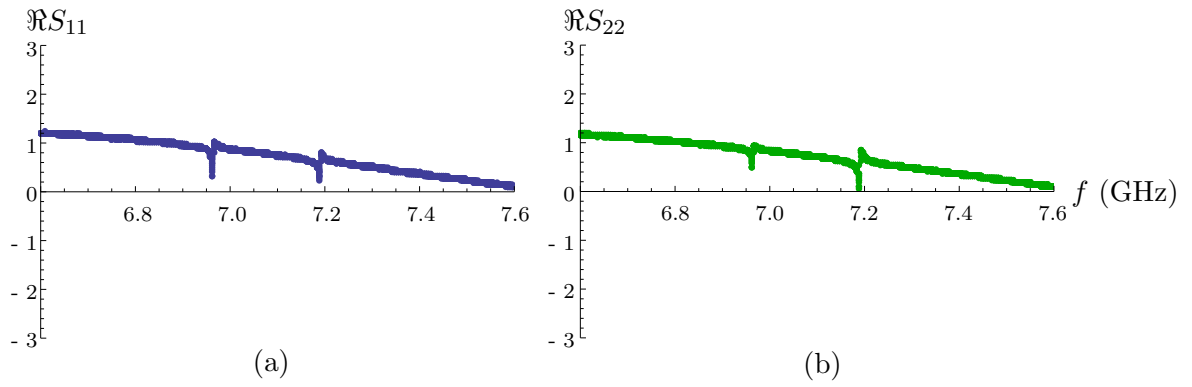
Figure 4.5: Measured $\Re S_{11}$ and $\Re S_{22}$ for sample M25 B1. Settings as follows: calibration with kit, $-2\,\mathrm{dBm}$ input power, averaging off.
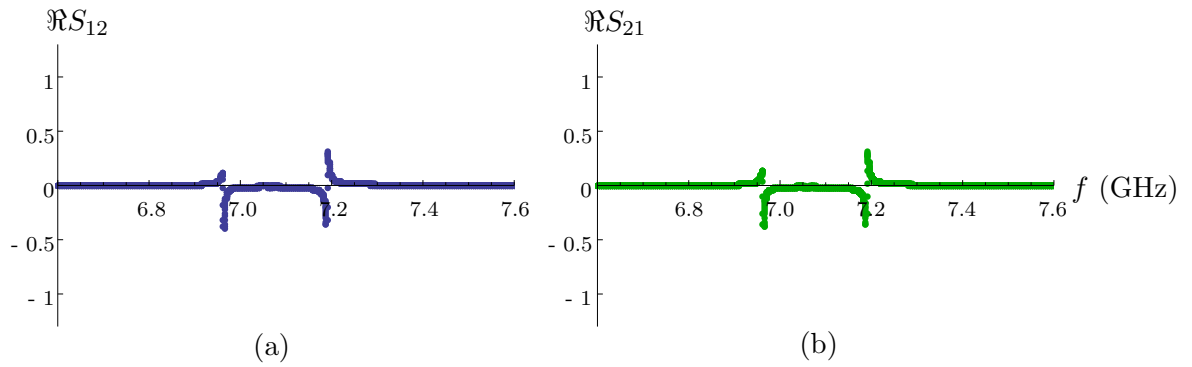

Figure 4.6: Measured $\Re S_{12}$ and $\Re S_{21}$ for sample M25 B1. Settings as in Figure 4.5.
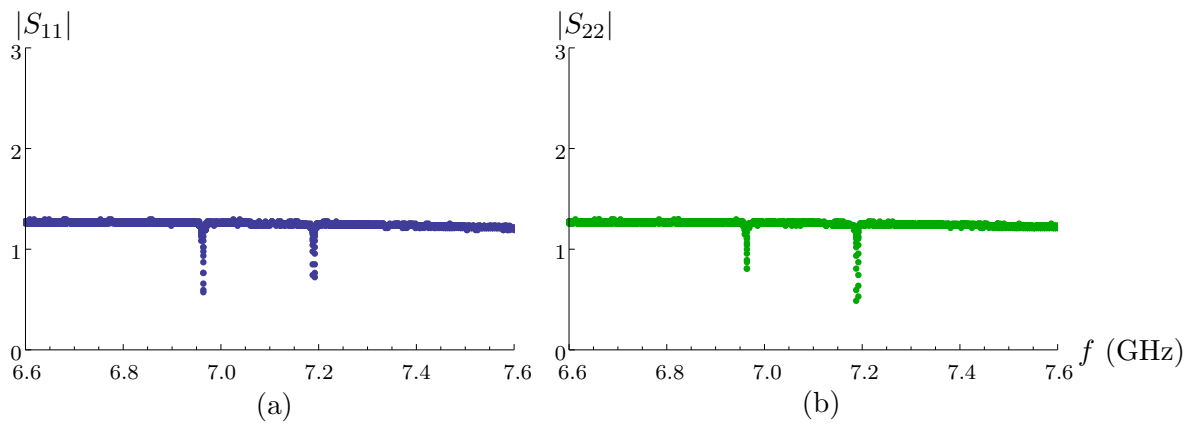
Figure 4.7: Measured $|S_{11}|$ and $|S_{22}|$ for sample M25 B1. Settings as in Figure 4.5.
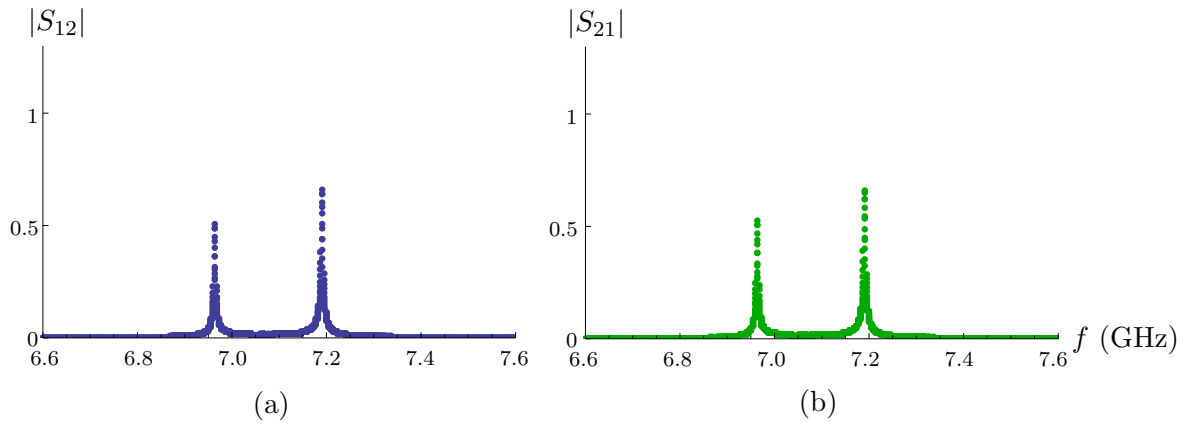

Figure 4.8: Measured $|S_{12}|$ and $|S_{21}|$ for sample M25 B1. Settings as in Figure 4.5.
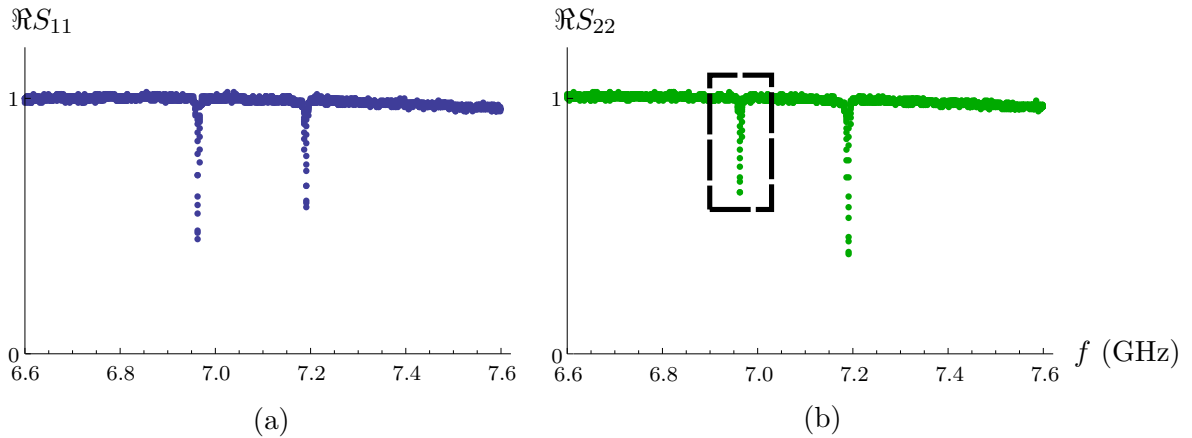
Figure 4.9: $\Re S_{11}$ and $\Re S_{22}$ from Figure 4.5 after post-correction. The dashed box indicates the resonance dip fitted in Figure 4.10.

expected from the design. Setting constraints on the parameters alleviated this problem a bit, but still did not produce stable, satisfactory fits. At a certain point I decided to abandon the idea of using ABCD matrices to fit the measurements and concentrated on fitting with input/output theory instead.

4.2 Extracted quantities

Before presenting the numerical results, it is worthwhile to reflect on whether the extracted quantities κ and γ belonging to different resonances (left and right) and scattering parameters ($\Re S_{11}$ and $\Re S_{22}$) should all be treated on equal footing. The input/output theory model for symmetrically coupled identical resonators indicates that they should. However, the measurements, because of the asymmetric resonances and the fact that $S_{11} \neq S_{22}$, signify that such an approach is questionable. The best way to tackle this problem would be to go back to input/output theory and try to develop a model which captures the aforementioned, initially unexpected observations. Such an attempt was made, see Equations 2.41 and 2.42, but turned out to be a dead-end in the sense that it failed to fully predict the observed asymmetry. A more promising idea is briefly discussed in Chapter 5.

4.2.1 Sample M25 A2

This was the first sample investigated. Inspection with an optical microscope showed that the sample was contaminated in the form of a large splotch on one of the two resonators as well as some dirt. Consequently, the observed asymmetry in the resonances was thought to be caused by the contamination and it was decided to move on to the next sample, sample M25 B1. Additionally, despite calibration the sample exhibited some strange behavior in S_{22}, see Figure 4.11b, which can probably be ascribed to the contamination. Therefore, only the results from fitting $\Re S_{11}$ are given.

Tables 4.1 and 4.2 contain all the extracted quantities. Each quantity is specified in the following manner: (average) $\pm$ (standard deviation). The results encompass a total of three measurements under the same settings (settings as in Figure 4.11). The only difference in the measurements was the frequency interval over which the scattering parameters were measured.
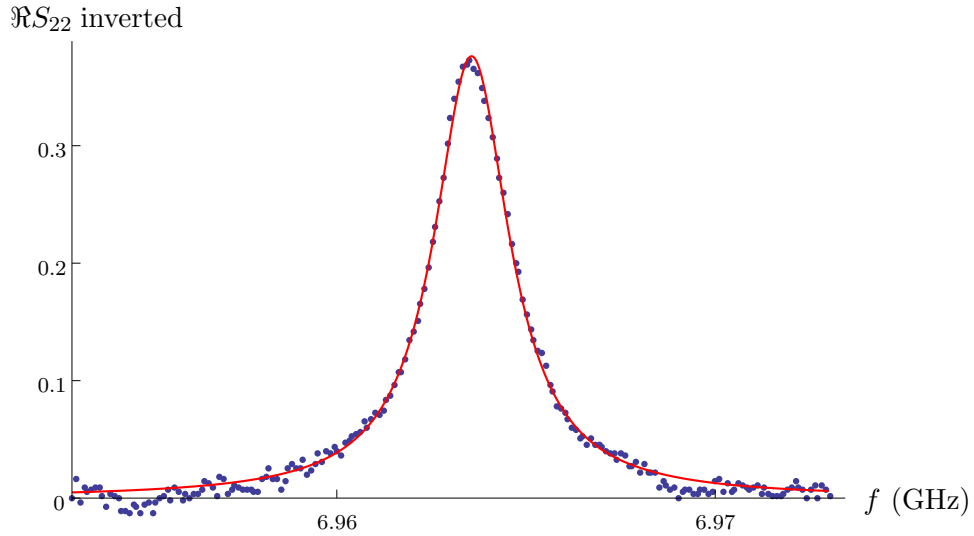
Figure 4.10: Example of fitting a resonance with a Lorentzian according to input/output theory. Fitting interval is $\pm 10\,\mathrm{MHz}$ around the resonance frequency.

In the first table, the left and right resonances are treated separately. In the second table, all resonances are considered at once, meaning that a single quantity $\kappa/\gamma/Q$ can be attributed to the sample.

The results show that the resonance frequencies f_{res} and therefore also J and f_0 practically do not change at all from measurement to measurement. These values are very stable. The same cannot be said for κ, γ and Q, especially in Table 4.2. This is not surprising because, after Table 4.1, κ, γ and Q are rather different for the two resonances, reflecting the observed asymmetry between them. Thus, when averaging over both resonances, as in Table 4.2, the variances of the aforementioned quantities will increase compared to what they were for each resonance individually. This phenomenon goes back to the remark at the beginning of this section.

Table 4.1: Extracted quantities for sample M25 A2 from various measurements. *Par.* refers to the fitted scattering parameter, *Res.* to the left or right resonance of the chosen scattering parameter.

Par.	Res.	f_{res}	$\kappa/2\pi$	$\gamma/2\pi$	Q
$\Re S_{11}$	left	$7.117\,\mathrm{GHz} \pm 0.22\,\mathrm{MHz}$	$1.27 \pm 0.01\,\mathrm{MHz}$	$1.71 \pm 0.09\,\mathrm{MHz}$	2391 ± 79
$\Re S_{11}$	right	$7.179\,\mathrm{GHz} \pm 0.09\,\mathrm{MHz}$	$2.31 \pm 0.02\,\mathrm{MHz}$	$1.46 \pm 0.08\,\mathrm{MHz}$	1905 ± 48

Table 4.2: Extracted quantities for sample M25 A2 from various measurements, taking both resonances from $\Re S_{11}$ into account (no distinction between left and right resonances).

$J/2\pi$	f_0	$\kappa/2\pi$	$\gamma/2\pi$	Q
$30.99 \pm 0.08\,\mathrm{MHz}$	$7.179\,\mathrm{GHz} \pm 0.09\,\mathrm{MHz}$	$1.79 \pm 0.52\,\mathrm{MHz}$	$1.59 \pm 0.16\,\mathrm{MHz}$	2148 ± 252

Lastly, using the extracted average values of J, f_0 and κ from Table 4.2 as well as Equa-
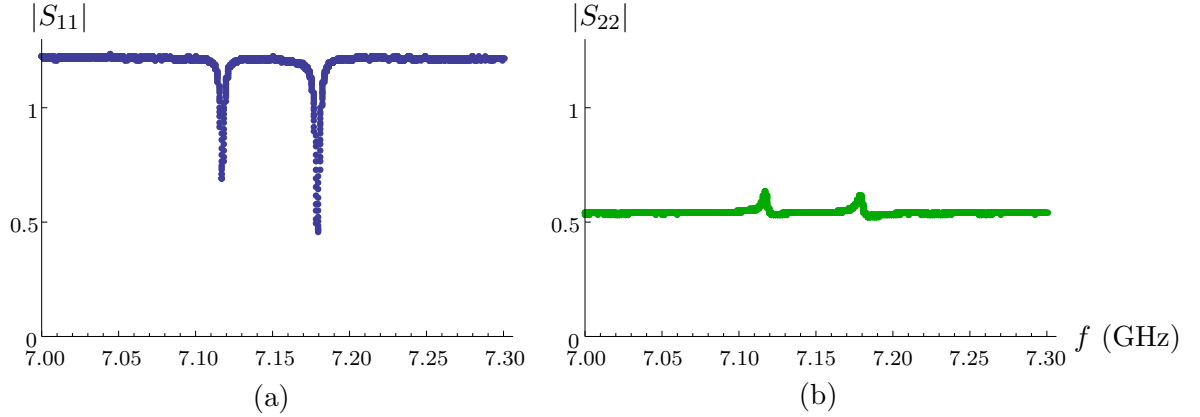
Figure 4.11: Measured $|S_{11}|$ and $|S_{22}|$ for sample M25 A2. Settings as follows: calibration with kit, -2 dBm input power, averaging off, IF bandwidth 600 kHz. Strangely, $|S_{22}|$ on resonance is greater than off resonance, likely because of contamination.

tions 2.39 and 2.40, one can estimate $C_{in/out}$ and C_m and compare them with the design specifications. We calculate, assuming $Z_0 = 50\,\Omega$, $C_{in/out} \approx 7.00$ fF and $C_m \approx 6.01$ fF. The design says that, approximately, $C_{in/out} = C_m = 6.6$ fF.

4.2.2   Sample M25 B1

This sample had, by design, a larger central coupling capacitor. Tables 4.3 and 4.4 contain all the extracted quantities. All of the comments regarding these quantities stated for the previous sample are valid here, too. The results incorporate four measurements, of which one pair had the same settings as in Figure 4.5, the two measurements differing only in the frequency interval considered. The other pair had the following settings: calibration with kit, -50 dBm input power, averaging with factor 100. The two measurements comprising this pair also only differed in the frequency interval considered.

Table 4.3: Extracted quantities for sample M25 B1 from various measurements. *Par.* refers to the fitted scattering parameter, *Res.* to the left or right resonance of the chosen scattering parameter.

Par.	Res.	f_{res}	$\kappa/2\pi$	$\gamma/2\pi$	Q
$\Re S_{11}$	left	6.964 GHz $\pm$ 0.17 MHz	1.42 $\pm$ 0.06 MHz	1.15 $\pm$ 0.03 MHz	2709 $\pm$ 87
$\Re S_{11}$	right	7.190 GHz $\pm$ 0.14 MHz	1.14 $\pm$ 0.06 MHz	1.60 $\pm$ 0.03 MHz	2623 $\pm$ 82
$\Re S_{22}$	left	6.964 GHz $\pm$ 0.09 MHz	0.89 $\pm$ 0.02 MHz	1.52 $\pm$ 0.03 MHz	2874 $\pm$ 10
$\Re S_{22}$	right	7.190 GHz $\pm$ 0.27 MHz	1.63 $\pm$ 0.10 MHz	1.02 $\pm$ 0.04 MHz	2723 $\pm$ 139

From Table 4.4 we calculate, assuming again $Z_0 = 50\,\Omega$, $C_{in/out} \approx 5.98$ fF and $C_m \approx 21.92$ fF. The design says that, approximately, $C_{in/out} = 6.6$ and $C_m = 22$ fF.

Comparing the measured resonance frequencies from sample M25 A2 with those from sample M25 B1, we see signs of the pinning phenomenon. The right resonance frequencies differ by around 11 MHz, the left by 153 MHz. What this means is that, when the central capacitor is increased, the resonance frequencies move further apart because the left frequency moves down, but the right one stays more or less where it is.

Table 4.4: Extracted quantities for sample M25 B1 from various measurements, taking both resonances from $\Re S_{11}$ as well as $\Re S_{22}$ into account (no distinction between left and right resonances).

$J/2\pi$	f_0	$\kappa/2\pi$	$\gamma/2\pi$	Q
$113.33 \pm 0.07\,\text{MHz}$	$7.190\,\text{GHz} \pm 0.21\,\text{MHz}$	$1.31 \pm 0.28\,\text{MHz}$	$1.32 \pm 0.26\,\text{MHz}$	$2712 \pm\ 130$

4.3   Discussion of asymmetry

For sample M25 B1, the fact that $S_{11} \neq S_{22}$ and the asymmetry in the resonances, Figures 4.7 and 4.8, point towards an asymmetry in the sample. Why is the origin of these occurrences very likely located on the sample or at least on the printed circuit board carrying the sample and not elsewhere (network analyzer and dipstick cables, connectors)? The reason is that I made a series of measurements where I rotated sample M25 B1, always in the same direction, so that a different pair of cables through the dipstick were used each time. Additionally, in a separate measurement I also exchanged the cables leading from the network analyzer to the dipstick, effectively interchanging the ports. In the former cases nothing changed regarding the asymmetry, whereas in the latter the resonances swapped (in $|S_{11}|$, the right resonance dipped below the left and vice versa in $|S_{22}|$, so that essentially S_{11} and S_{22} were exchanged). These observations are consistent with the notion that the asymmetry originates from the sample.

In order to shed some light on what could cause the asymmetry, I ran some small simulations in Microwave Office. Below is a list of potential causes:

- The two resonators have different resonance frequencies: this can happen because the resonators have different geometries (lengths, widths) and/or effective electric permittivities (geometry dependent). Then, the equivalent single resonator fundamental resonance frequencies are not the same for the two resonators. Simulations show that length differences as small as 1% already have a significant impact and reproduce the observed asymmetry very nicely.

- Unequal input/output coupling capacitors: $C_{in} \neq C_{out}$. See Figure 2.8. Leads to $S_{11} \neq S_{22}$. The asymmetry in the resonances (unequal dips) is more pronounced when the central coupling capacitor is smaller. At $C_m = 22\,\text{fF}$, not the likely source because the input/output capacitors, set ideally to 6.6 fF, have to disagree on the order of a femtofarad or more.

- Mismatches in the characteristic impedances: can be because the resonators are not identical to each other or due to imperfections in the waveguides and connectors on the printed circuit board. Not that likely because deviations on the order of several ohms and above are required.

- Parasitic capacitors and inductors: variations in the number and/or geometry of the bond wires connecting the sample to the printed circuit board could bring about asymmetric parasitic capacitors and/or inductors. Alternatively, the parasitic components could manifest themselves at the connectors. Asymmetric parasitic capacitors can be considered for by combining them with the input/output capacitors, leading to the first point in this list. Similarly, parasitic inductors lead to $S_{11} \neq S_{22}$,

but the resonances, when looking at say $|S_{11}|$ or $|S_{22}|$ individually, are not very asymmetric. The influence is also rather weak, needing inductances of several nanohenries. In comparison, in Ref. [14] it is stated that a bond wire has an approximate inductance per unit length of $1\,\text{nH/mm}$.

In summary, differences in the resonance frequencies of the resonators appear to be the most likely candidate for the observed phenomena. Of course, in reality, a combination of diverse factors is probably to blame.

4.4   Brief look at $N = 4$ sample

Sample M25 M1 featured four coupled resonators. By design, the three capacitors coupling the resonators to each other were the same. Figure 4.12a shows a measurement of the transmission through the sample. Now, there are four fundamental resonance frequencies. Note the strong asymmetry in the resonances. Figure 4.12b is a Microwave Office simulation, where it was assumed that all resonators and coupling capacitors are identical, i.e., the sample is completely symmetric. Additionally, $S_{11} = S_{22}$, but again the resonances are asymmetric. It seems that, in this case, the asymmetry in the resonances is an inherent property of the sample.
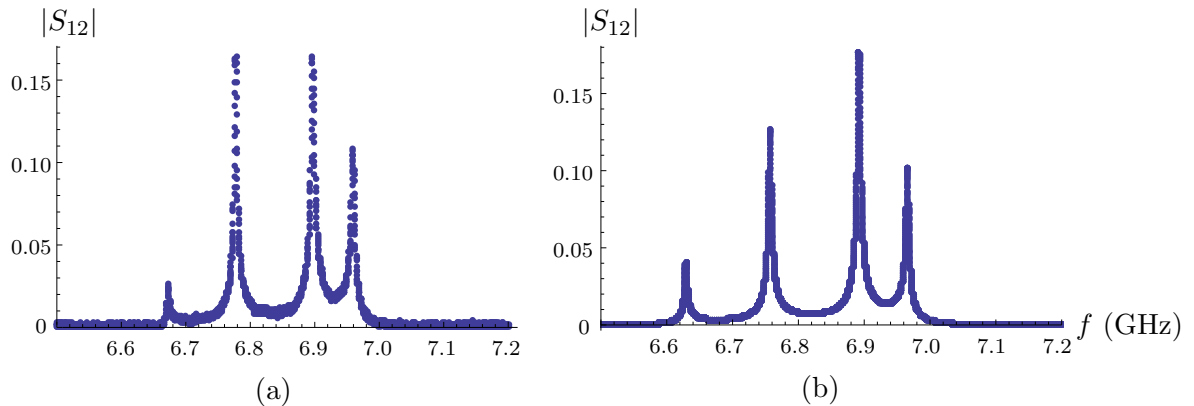

Figure 4.12: Measured, left, $|S_{12}|$ and simulated, right, $|S_{12}|$ for sample M25 M1. Measurement settings as follows: calibration with kit, $-4\,\text{dBm}$ input power, averaging off.

Finally, simulations also confirm the pinning of the rightmost resonance frequency, independent of the three coupling capacitors.

Chapter 5

Conclusion and outlook

In summary, during the course of this semester thesis I delved into the topic of coupled microwave resonators. The focus was mostly on two samples, each having two coupled resonators, but different central capacitors. From a theoretical standpoint, I tried to understand how the resonances come about as well as how to describe the overall transmission and reflection in the form of scattering parameters. I pursued two strategies: a macroscopic description with ABCD matrices from classical microwave theory and a microscopic description rooted in input/output theory, a quantum mechanical approach to understanding coupled optical resonators. Experimentally, I performed low-temperature dipstick measurements to determine the scattering parameters. Once the measurements were completed, the gathered data was analyzed and relevant quantities extracted. The initially unexpected asymmetry present in the samples was scrutinized through further measurements and several simulations in order to shed some light on its origins.

There are a lot of possibilities for expanding on this semester thesis. As part of the overarching search for Majorana-like modes of light in coupled resonators at the Quantum Device Lab, the next logical step would be the qubit integration. Additionally, samples containing higher numbers of coupled resonators will probably need to be studied, both theoretically and experimentally. The $N = 4$ sample which I briefly investigated seems like a good starting point.

In the following, a list of untested, but potentially interesting ideas and improvements regarding this thesis are presented. They were not implemented either due to time constraints or because I only become aware of them towards the very end of the thesis.

- Higher harmonics: examine the higher harmonics in the transmission and reflection. Is it possible to obtain any useful information from them?

- Input/output theory: develop a simple model within input/output theory which successfully predicts $S_{11} \neq S_{22}$ together with the observed asymmetry in the resonances. It was suggested to me that the corresponding Hamiltonian, which should replace the one given in Equation 2.28, is

$$H = \omega_1 a^\dagger a + \omega_2 b^\dagger b + J a^\dagger b + J b^\dagger a, \tag{5.1}$$

  with $\Delta = |\omega_2 - \omega_1| \gg J$. Here, ω_1 and ω_2 are the resonance frequencies of the left and right resonator, respectively. These two resonators, which together comprise the dimer, are assumed to be different, i.e., asymmetric, and therefore their resonance frequencies are different.

- Fitting in the complex plane: instead of fitting, say, $\Re S_{11}$, fit S_{11} directly in the complex plane. One advantage of such an approach is that the somewhat tedious and inconsistent manual post-correction would not be necessary any more, at least not in the form which I implemented.

- Terminate unused waveguides: present on the samples are flux and charge lines. In my measurements, these lines were left unconnected. This could potentially produce additional reflections, impacting the transmission and reflection through the coupled resonators. To be on the safe side, all unused ports should be terminated in matched $50\,\Omega$ loads to prevent reflections.

Chapter 6

Acknowledgements

I would like to express my gratitude to Prof. Andreas Wallraff for allowing me to write a semester thesis at the Quantum Device Lab. Additionally, I would like to thank my supervisor, Milan Allan, for his patience, help and guidance.

Appendix A

Project file directory

All files are located on qudev in USERS\Matija\semester_thesis. The table below lists the foldes therein and their contents:

Table A.1: Project file directory.

Folder	Content
doc	papers and thesis relevant for the project
measurements	measurement data acquired in the lab
mathematica	code written in Mathematica; mostly related to input-output theory
matlab	code writen in MATLAB; mostly related to ABCD matrix formalism
microwave office	simulations in Microwave Office
report	files pertaining to the report

Bibliography

[1] R. J. Schoelkopf and S. M. Girvin. Wiring up quantum systems. *Nature*, 451:664–669, 2008.

[2] A. Blais, R.-S. Huang, A. Wallraff, S. M. Girvin, and R. J. Schoelkopf. Cavity quantum electrodynamics for superconducting electrical circuits: An architecture for quantum computation. *Phys. Rev. A*, 69(6):062320–14, June 2004.

[3] Jens Koch, Terri M. Yu, Jay Gambetta, A. A. Houck, D. I. Schuster, J. Majer, Alexandre Blais, M. H. Devoret, S. M. Girvin, and R. J. Schoelkopf. Charge-insensitive qubit design derived from the Cooper pair box. *Phys. Rev. A*, 76(4):042319, 2007.

[4] M. Göppl, A. Fragner, M. Baur, R. Bianchetti, S. Filipp, J. M. Fink, P. J. Leek, G. Puebla, L. Steffen, and A. Wallraff. Coplanar waveguide resonators for circuit quantum electrodynamics. *J. Appl. Phys.*, 104:113904, 2008.

[5] A. Wallraff, D. I. Schuster, A. Blais, L. Frunzio, R.-S. Huang, J. Majer, S. Kumar, S. M. Girvin, and R. J. Schoelkopf. Strong coupling of a single photon to a superconducting qubit using circuit quantum electrodynamics. *Nature*, 431:162–167, 2004.

[6] Rodney Loudon. *The Quantum Theory of Light*. Oxford U, 2000.

[7] D. Underwood, W. Shanks, J. Koch, and A. A. Houck. Low-disorder microwave cavity lattices for quantum simulation with photons. *arXiv:1203.5363v1*, 2012.

[8] M.J. Hartmann, F.G.S.L. Brandao, and M.B. Plenio. Quantum many-body phenomena in coupled cavity arrays. *Laser & Photon. Rev.*, 2(6):527–556, 2008.

[9] Andrew A. Houck, Hakan E. Tureci, and Jens Koch. On-chip quantum simulation with superconducting circuits. *Nat. Phys.*, 8(4):292–299, April 2012.

[10] C.-E. Bardyn and A. İmamoğlu. Majorana-like modes of light in a one-dimensional array of nonlinear cavities. *Phys. Rev. Lett.*, 109:253606, Dec 2012.

[11] Lukas Korosec. Design of nonlinear resonator arrays in superconducting circuits. Master's thesis, ETH Zurich, 08 2012.

[12] L. Heinzle. Transmon qubit design for a cavity dimer in circuit qed. Semester thesis, ETH Zurich, 2013.

[13] David M. Pozar. *Microwave engineering*. John Wiley & Sons, Inc., 4th ed. edition, 2011.

[14] D. I. Schuster. *Circuit Quantum Electrodynamics*. PhD thesis, Yale University, 2007.

[15] D. F. Walls and G. J. Milburn. *Quantum Optics*. Springer Verlag, Berlin, 2 edition, 2008.

[16] Christopher Eichler. *Experimental Characterization of Quantum Microwave Radiation and its Entanglement with a Superconducting Qubit*. PhD thesis, ETH Zurich, 2013.

[17] Gebhard Littich. Superconducting mach-zehnder interferometers for circuit quantum electrodynamics. Master's thesis, ETH Zurich, 04 2009.

[18] Jen-Hao Yeh and Steven M. Anlage. In situ broadband cryogenic calibration for two-port superconducting microwave resonators. *Rev. Sci. Instrum.*, 84(3):034706–8, March 2013.